IMPELLER BURST ANALYSIS AND VALIDATION

ÇARK İNFİLAK ANALİZİ VE VALİDASYONU

ALPER SARITEN

PROF. DR. BORA YILDIRIM

Supervisor

Submitted to

Graduate School of Science and Engineering of Hacettepe University

as a Partial Fulfillment to the Requirements

for the Award of the Degree of Master of Science

in Mechanical Engineering

December 2022

ABSTRACT

IMPELLER BURST ANALYSIS AND VALIDATION

Alper Sarıten

Master of Science, Mechanical Engineering

Supervisor: Prof. Dr. Bora YILDIRIM

December 2022, 94 pages

The rotating parts in gas turbines are expected to operate safely under different loads, such as high centrifugation, temperature, and pressure. Due to the high centrifugal forces generated at high rotational speeds, there is a risk of the parts losing their structural integrity and burst, then damaging both the engine and the aircraft. For this reason, it is vital to calculate the burst speed of related parts accurately. In this study, burst speeds are calculated for two different impeller geometries using different damage criteria. The finite element study is performed with ANSYS Workbench 2020 R2 software. Finally, the manufactured parts are tested, and the actual burst speeds are found and compared with the values obtained by numerical methods.

Keywords: burst, impeller, finite element method, ANSYS, fracture, test, compressor, plasticity, deformation

ÖZET

ÇARK İNFİLAK ANALİZİ VE VALİDASYONU

Alper Sarıten

Yüksek Lisans, Makina Mühendisliği Bölümü

Danışman: Prof. Dr. Bora YILDIRIM

Kasım 2022, 94 sayfa

Gaz türbinleri içerisindeki dönen parçaların yüksek santrifüj, sıcaklık ve basınç gibi farklı yükler altında güvenli bir şekilde çalışması beklenir. Yüksek dönme hızlarında oluşan yüksek santrifüj kuvvetler nedeniyle parçaların yapısal bütünlüğünü kaybederek infilak edip motora ve hava aracına zarar verme riski vardır. Bu nedenle infilak olayının gerçekleşeceği hızın isabetli bir şekilde hesaplanması oldukça önemlidir. Bu çalışmada, iki farklı çark geometrisi için, farklı hasar kriterleri kullanılarak, infilak hızları hesaplanmıştır. Hesaplar için gereken sonlu elemanlar analizleri ANSYS Workbench 2020 R2 kullanılarak gerçekleştirilmiştir. Daha sonra imal edilen parçalar test edilerek gerçek infilak hızları bulunmuş ve nümerik yöntemlerle elde edilen değerlerle karşılaştırılmıştır.

Keywords: infilak, çark, sonlu elemanlar methodu, ANSYS, hasar, test, kompresör, plastisite, deformasyon

ACKNOWLEDGEMENTS

I would like to sincerely thank my supervising professor Dr. Bora Yıldırım for his guidance, support, and encouragement throughout my research in every aspect. My gratitude goes to the committee members: Dr. Barış Sabuncuoğlu, Dr. Hasan Basri Ulaş, Dr. Mehmet Okan Görtan and Dr. Can Ulaş Doğruer.

For their mentoring and guidance special thanks to Burak Balcı and Alican Kutmaral, who were always there.

Most of all, thanks to my family, who made this study possible with their love, support, and faith in me. Also, I am grateful and thankful to my friends for their endless patience and support.

CONTENTS

Page

ABSTRACT i
ÖZET ii
ACKNOWLEDGEMENTS iii
CONTENTS iv
TABLES vii
FIGURES viii
ABBREVIATIONS xii
1. INTRODUCTION 1
1.1. Gas Turbines and Rotating Components 1
1.2. Burst Failure 5
1.3. Purpose of the Study 8
2. THEORY 12
2.1. Material Behavior 12
2.1.1. Elastic Field 13
2.1.2. Plastic Field 15
2.2. Material Models 16
2.2.1. Ramberg-Osgood Material Model 16
2.2.2. Johnson-Cook Material Model 18
2.2.3. Johnson-Cook Material Model 18
2.3. Experimental Tensile Tests 19
2.4. Finite Element Analysis 20
2.4.1. Brief History of FEM and Preferred Software 20
2.4.2. Finite Element Analysis Theory 21
2.5. Explicit Dynamic Analysis Theory 23
2.6. Fracture Criteria 25
2.6.1. Robinson's Criteria 25
2.6.2. Critical Strain Through Cross-section Criteria 25

2.6.3. Explicit Dynamic Analysis Criterion 26
3. METHODOLOGY 27
3.1. Material Data 27
3.1.1. Experimental Tensile Tests 27
3.1.2. Johnson-Cook Material Model Parameters 29
3.1.3. Johnson-Cook Failure Model Parameters 29
3.2. Preprocessing Model 30
3.2.1. Definition of PLANE183 30
3.2.2. Definition of PLANE164 31
3.3. Static Structural Analysis 32
3.3.1. Elastic Analysis 32
3.3.2. Elastoplastic Analysis 34
3.4. Explicit Dynamic Analysis 34
3.5. Test Setup 36
4. RESULTS 40
4.1. Numerical Results 40
4.1.1. Results of Geometry-1 40
4.1.1.1. Elastic Analysis Results 40
4.1.1.2. Elastoplastic Analysis Results 42
4.1.1.3. Explicit Dynamic Analysis Results 44
4.1.2. Results of Geometry-2 48
4.1.2.1. Elastic Analysis Results 48
4.1.2.2. Elastoplastic Analysis Results 49
4.1.2.3. Explicit Dynamic Analysis Results 51
4.2. Fracture Criteria Results 55
4.3. Experimental Results 57
4.3.1. Experimental Results of Geometry-1 57
4.3.2. Experimental Results of Geometry-2 60
4.4. Comparison of Numerical and Experimental Results 63
4.4.1. Comparison of Results for Geometry-1 63

4.4.2. Comparison of Results for Geometry-2 66
5. CONCLUSIONS 70

TABLES

Page

Table 1.1 Rotor Integrity Conditions 8

Table 3.1 Constants of the Material Model for Ti64..... 29

Table 3.2 Constants of the Damage Law for Ti64 30

Table 4.1 Burst Margin Calculations of Geometry-1 66

Table 4.2 Burst Margin Calculations of Geometry-2 69

FIGURES

		Page
Figure 1.1	Gas Turbine Configurations Used in Aviation	2
Figure 1.2	Turboshaft Engine	3
Figure 1.3	Impeller	4
Figure 1.4	Materials Used in a Turbofan Engine	5
Figure 1.5	Fragments of Fractured Disk	6
Figure 1.6	Burst Failure and Aftermath	7
Figure 1.7	Aircraft Damaged by a Fragment After Burst Failure	7
Figure 1.8	Manufactured Test Part, Geometry-1	9
Figure 1.9	Cross-section of Geometry-1	10
Figure 1.10	Manufactured Test Part, Geometry-2	10
Figure 1.11	Cross-section of Geometry-2	11
Figure 2.1	Material Behaviors	12
Figure 2.2	Poisson's Effect	13
Figure 2.3	Stress-Strain Curve	15
Figure 2.4	Isotropic and Kinematic Hardening	16
Figure 2.5	Ramberg-Osgood Equation Offset Line	17
Figure 2.6	Engineering and True Stress-Strain Curves	20
Figure 2.7	Linear Static Analysis Approach	22
Figure 2.8	Non-linear Static Analysis Approach	23
Figure 3.1	Test Specimen Before and After Tensile Test	28
Figure 3.2	True Stress – Strain Curve of Geometry-1 [Normalized]	28
Figure 3.3	True Stress – Strain Curve of Geometry-2 [Normalized]	29
Figure 3.4	Geometry properties of PLANE183	31
Figure 3.5	Geometry properties of SOLID164	31
Figure 3.6	Elastic & Elastoplastic Analysis Mesh Detail and Boundary Conditions of Geometry-1	32

Figure 3.7 Elastic & Elastoplastic Analysis Mesh Detail and Boundary Conditions of Geometry-2 33
Figure 3.8 Specific Regions of Geometries 33
Figure 3.9 Explicit Dynamic Analysis Boundary Conditions of Geometry-1 34
Figure 3.10 Explicit Dynamic Analysis Mesh Details of Geometry-1 35
Figure 3.11 Explicit Dynamic Analysis Boundary Conditions of Geometry-2 35
Figure 3.12 Explicit Dynamic Analysis Mesh Details of Geometry-2 36
Figure 3.13 Spin Rig 37
Figure 3.14 Geometry-1 Assembled on the Spin Rig 37
Figure 3.15 Geometry-2 Assembled on the Spin Rig 38
Figure 3.16 Oven Assembled on the Spin Rig 38
Figure 3.17 Speed Profile of Geometry-1 39
Figure 3.18 Speed Profile of Geometry-2 39
Figure 4.1 Normalized Radial and Axial Stress Plots from Elastic Analysis 41
Figure 4.2 Normalized Tangential and Equivalent Stress Plots from Elastic Analysis 41
Figure 4.3 Normalized Total Deformation and Total Strain Plots from Elastic Analysis 42
Figure 4.4 Normalized Radial and Axial Stress Plots from Elastoplastic Analysis 43
Figure 4.5 Normalized Tangential and Equivalent Stress Plots from Elastoplastic Analysis 43
Figure 4.6 Normalized Total Deformation and Total Strain Plots from Elastic Analysis 44
Figure 4.7 Normalized Equivalent Stress (Crack Initiation) 45
Figure 4.8 Normalized Equivalent Stress (Crack Growth) 45
Figure 4.9 Normalized Equivalent Stress (Fracture) 46
Figure 4.10 Normalized Plastic Strain (Crack Initiation) 46
Figure 4.11 Normalized Plastic Strain (Crack Growth) 47
Figure 4.12 Normalized Plastic Strain (Fracture) 47
Figure 4.13 Normalized Radial and Axial Stress Plots from Elastic Analysis 48

Figure 4.14 Normalized Tangential and Equivalent Stress Plots from Elastic Analysis..... 49
Figure 4.15 Normalized Total Deformation and Total Strain Plots from Elastic Analysis..... 49
Figure 4.16 Normalized Radial and Axial Stress Plots from Elastoplastic Analysis 50
Figure 4.17 Normalized Tangential and Equivalent Stress Plots from Elastoplastic Analysis..... 50
Figure 4.18 Normalized Total Deformation and Total Strain Plots from Elastic Analysis..... 51
Figure 4.19 Normalized Equivalent Stress (Crack Initiation) 52
Figure 4.20 Normalized Equivalent Stress (Crack Growth) 52
Figure 4.21 Normalized Equivalent Stress (Fracture) 53
Figure 4.22 Normalized Plastic Strain (Crack Initiation)..... 53
Figure 4.23 Normalized Plastic Strain (Crack Growth)..... 54
Figure 4.24 Normalized Plastic Strain (Fracture) 54
Figure 4.25 Locations Past Critical Strain Value, Geometry-1 55
Figure 4.26 Locations Past Critical Strain Value, Geometry-1 56
Figure 4.27 Locations Past Critical Strain Value, Geometry-2 56
Figure 4.28 Locations Past Critical Strain Value, Geometry-2 57
Figure 4.29 Fragments of Geometry-1 58
Figure 4.30 Crack Initiation..... 59
Figure 4.31 Crack Growth 59
Figure 4.32 Fracture 60
Figure 4.33 Fragments of Geometry-2 61
Figure 4.34 Fragments of Geometry-2 61
Figure 4.35 First Crack Initiation 62
Figure 4.36 Second Crack Initiation 62
Figure 4.37 Fracture 63
Figure 4.38 Crack Initiation..... 64
Figure 4.39 Crack Growth 65

Figure 4.40 Fracture 66
Figure 4.41 Crack Initiation 67
Figure 4.42 Crack Growth 68
Figure 4.43 Fracture 69

ABBREVIATIONS

Symbols

σ	:	Engineering Stress
E	:	Young's Modulus (Modulus of Elasticity)
ε, e	:	Engineering Strain
e_x, e_y, e_z	:	Strains on Direction x, y, z
$\sigma_x, \sigma_y, \sigma_z$	:	Normal Stresses on Plane x, y, z
σ_p	:	Principal Stress
v	:	Poisson's Ratio
F	:	Normal Force
A_0	:	Original Area
l_0	:	Original Length
l_i	:	Instantaneous Length
σ_T	:	True Stress
ε_T	:	True Strain
K, n	:	Ramberg-Osgood Constants
m	:	Mass
ω	:	Angular Velocity
r_0	:	Original Radius
r	:	Radius
u	:	Radial Deflection
ϕ_v	:	Centrifugal Force

Abbreviations

RPM	:	**R**evolutions **p**er **M**inute
FEM	:	**F**inite **E**lement **M**ethod
Ti 64	:	**T**i- **6**V- **4**Al Alloy

Ansys WB	:	**A**nsys **W**ork**B**ench Finite Element Software
EASA	:	**E**uropean **A**viation **S**afety **A**gency
FAA	:	**F**ederal **A**viation **A**dministration

1. INTRODUCTION

1.1. Gas Turbines and Rotating Components

A gas turbine is a type of continuous and internal combustion engine and is defined as "*The power plant, which produces a great amount of energy depending its size and weight.*" [1] There are different configurations of gas turbine engines used in the aviation industry, like turboshafts, turbojets, turbofans, turboprops, etc. (Figure 1.1)

Turbojet engines are widely used in military aviation and rockets because of their high speed and performance. It consists of a compressor, turbine, combustion chamber, and exhaust nozzle.

Turbofan engines are commonly used in civil aviation due to their low specific fuel consumption and high efficiency at lower cruise speeds. Its structure is very similar to a turbojet engine except for a fan attached to the front of it. The fan helps to suck more air than a turbojet engine. Not all of the air sucked by the fan is sent to the core engine some of it passes around the engine and creates additional thrust.

Turboprop engines have higher efficiency in slow cruise speeds because of that mostly used on cargo aircrafts. Its configuration consists of a propeller attached to the core engine through a reduction gear. The propeller creates the required thrust to move the aircraft, and the reduction gear reduces the rotating speed of the propeller and increases torque.

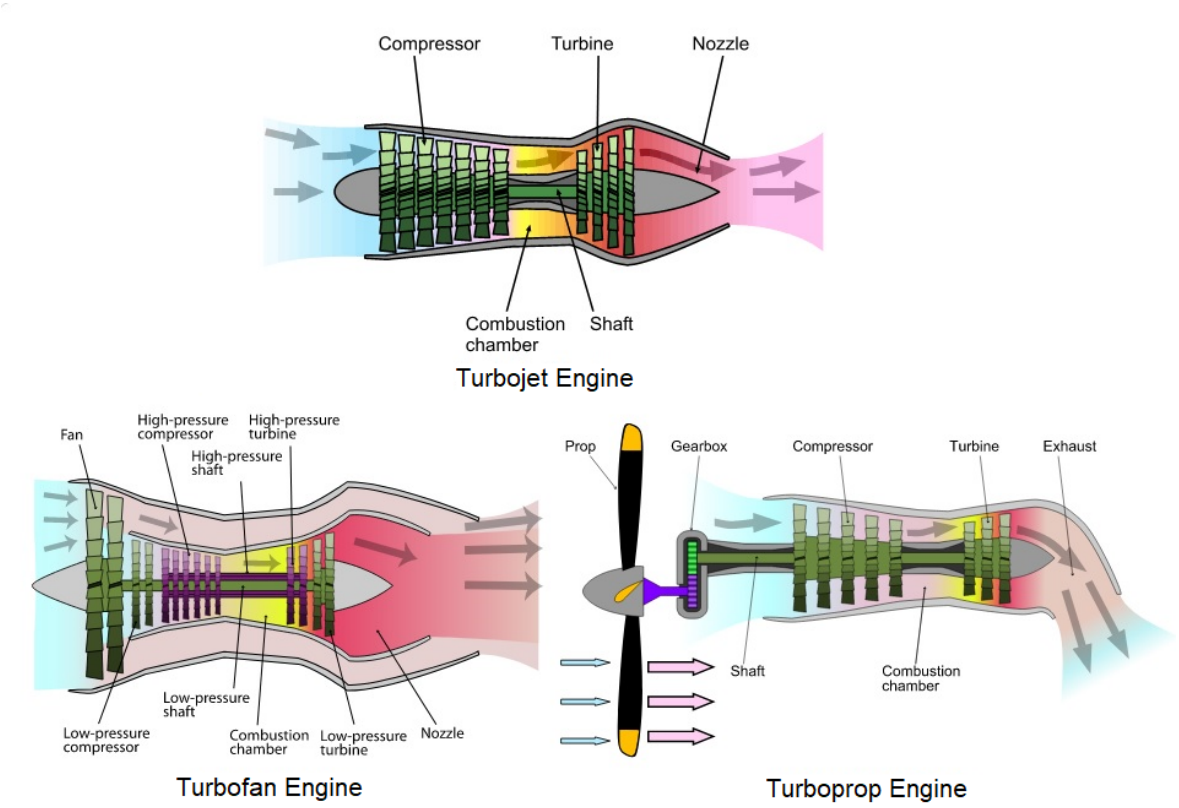

Figure 1.1 Gas Turbine Configurations Used in Aviation

Turboshaft engines have a similar configuration to turboprop engines but have a shaft attached to the core engine instead of the propeller and reduction gear.

Gas turbines may have different configurations, but the core engine section is the common point.

The main modules of a typical gas turbine core engine are:

- a gas compressor
- a combustor
- a turbine on the same shaft as the compressor. (Figure 1.2)

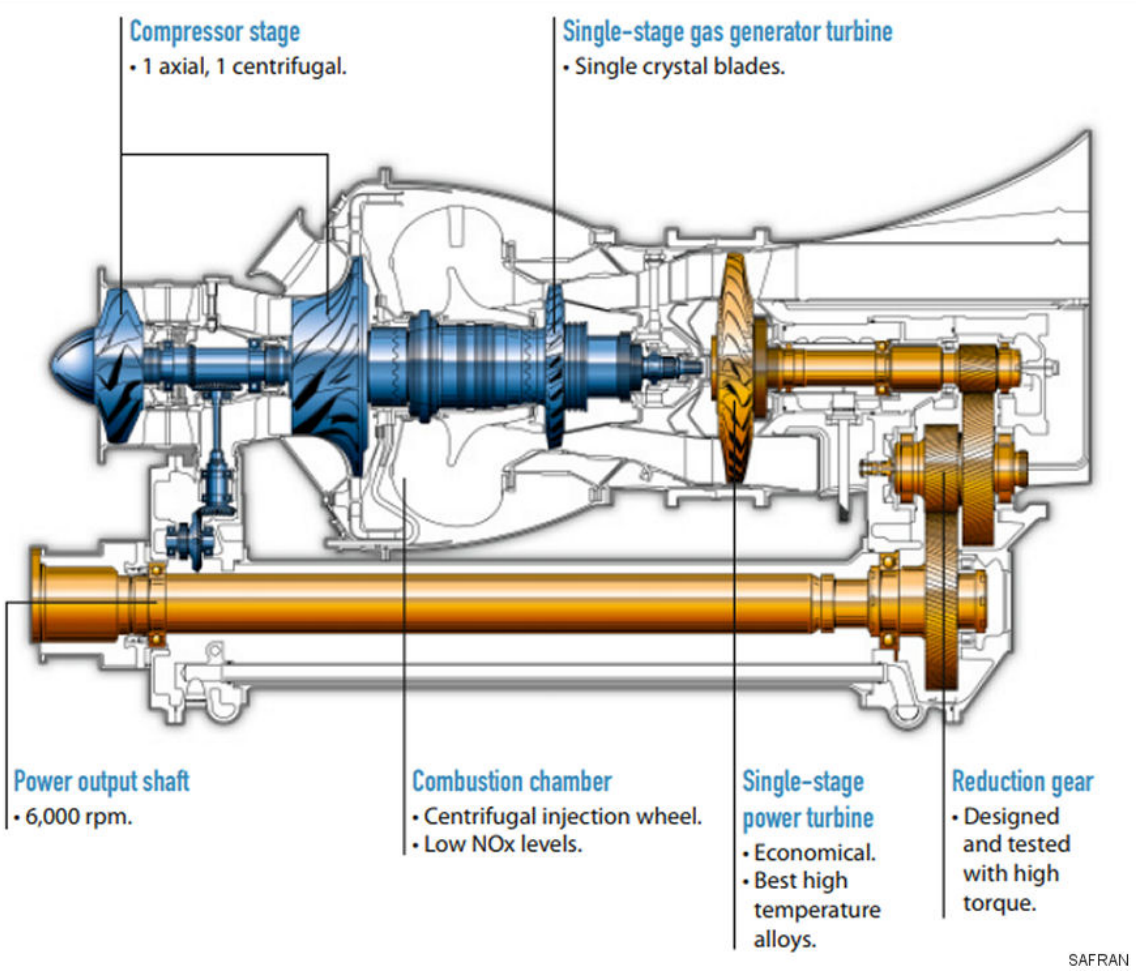

Figure 1.2 Turboshaft Engine

[2]

The compressor section is responsible for pressurizing air that comes from the inlet section and sending pressurized air to the combustion chamber. Compressors consist of a row of stationary and a row of rotating parts. Rotating parts transfer kinetic energy to the air, and stationary parts convert the kinetic energy of the fluid to pressure. The compressor section may have a radial or axial configuration. The radial compressor is, also called centrifugal compressor, extensively used in small gas turbines owing to the advantage of high-pressure ratio per stage and smaller sizes. The rotating part of the radial compressor is called impeller. (Figure 1.3)

Figure 1.3 Impeller

[3]

Different modules on the engine operate under various loads. For example, maximum pressure and temperature values occur in the combustion chamber. In the turbine section, rotating parts work under high centrifugal load in addition to high pressure and temperatures. The compressor module works under low temperatures compared to the turbine and combustion chamber modules.

All of these differences between operating environments affect materials used in modules. In the compressor module, titanium alloys are widely used on account of their low density, high strength and excellent resistance against corrosion. In the modules that operate under high

temperatures generally, nickel alloys are preferred because of the ability to keep mechanical properties at high temperatures. In Figure 1.4, materials used in a turbofan engine are shown.

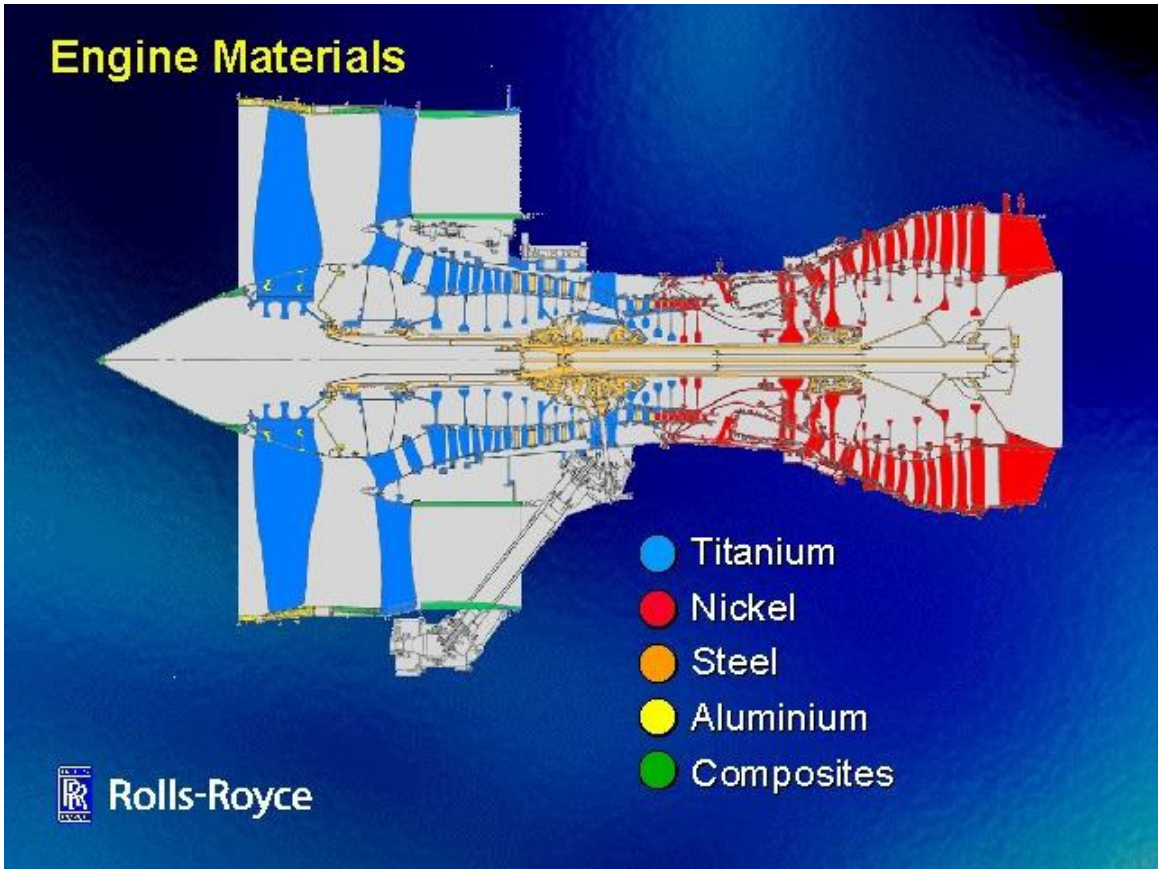

Figure 1.4 Materials Used in a Turbofan Engine

[4]

1.2. Burst Failure

Rotating parts of a gas turbine operate under severe centrifugal, pressure, and temperature loads not only in standard operating limits but also beyond these limits needed to withstand these loads. Rotating parts may start to spin higher than normal working speeds due to some failure on the engine, and this situation is called Overspeed.

Centrifugal force creates an inertial load on the rotating disks, and the inertial load can create a large deflection on the disc and a failure may occur due to elastic instability. [5] Strains and radial deflections increase in proportion to the angular velocity. If the initial radius of

the rotating disc is denoted as r_0 and radial deflection u, the radius of the disc under rotation can be expressed with:

$$r = u + r_0 \tag{1}$$

It is mentioned that radial deflection is caused by centrifugal force. The relationship between centrifugal force, angular velocity, and disc radius can be expressed with:

$$r = u + r_0 \tag{2}$$

It can be seen that the centrifugal force ϕ_v increases as angular velocity increases. On the other hand, with the effect of centrifugal force radius of the disc increases and causes additional centrifugal load. Finally, the part cannot handle centrifugal forces at a certain point, and burst failure occurs. (Figure 1.5)

Figure 1.5 Fragments of Fractured Disk

[6]

Burst failure is a significant safety concern for aircrafts due to high-energy fragments. These parts can destroy the engine and even the fuselage of aircraft. (Figure 1.6 & Figure 1.7)

Figure 1.6 Burst Failure and Aftermath

[7]

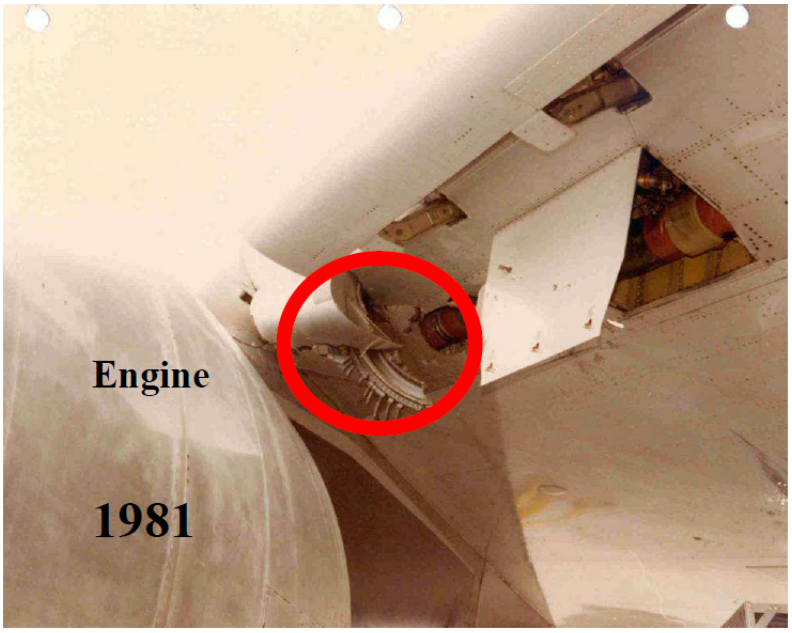

Figure 1.7 Aircraft Damaged by a Fragment After Burst Failure

[8]

Due to this risky situation, civil aviation authorities have strict regulations to guarantee the integrity of rotating parts. Two leading aviation authorities, European Aviation Safety Agency (EASA) and Federal Aviation Administration (FAA), release requirements and gas turbine engines used in a civil aircraft must meet integrity criteria in an Overspeed condition. [9], [10] Summary of the requirements for different engine conditions released by the FAA and EASA are summarized in Table 1.1.

EASA CS-E 840	**FAR 33.27**
120% of the maximum permissible rotor speeds associated with any of the ratings except OEI ratings of less than 2 1/2-minutes.	120 percent of its maximum permissible r.p.m. if tested on a rig and equipped with blades or blade weights.
115% of the maximum permissible rotor speeds associated with any OEI ratings of less than 2 1/2-minutes.	115 percent of its maximum permissible r.p.m. if tested on an engine.
105% of the highest rotor speed that would result from the failure of the component or system which is the most critical with respect to overspeeding.	105 percent of the highest speed that would result from failure of the most critical component or system in a representative installation of the engine.
100% of the highest rotor speed that would result from the failure of the component or system which, in a representative installation of the engine, is the most critical with respect to overspeeding when operating at any OEI ratings of less than 2 1/2-minutes.	The highest speed that would result from the failure of any component or system in a representative installation of the engine, in combination with any failure of a component or system that would not normally be detected during a routine preflight check or during normal flight operation.

Table 1.1 Rotor Integrity Conditions

Due to all of these safety concerns and regulations, calculating the burst speed of a rotating component is a critical task.

1.3. Purpose of the Study

Due to safety concerns, it is crucial to determine the burst speed of critical rotating parts used in an engine. However, spin tests have long lead times and high costs, and because of that,

before the test, it is better to calculate the expected burst speed accurately using numerical methods.

This study aimed to compare calculated burst speeds and test results. Two different impeller geometries are analyzed with the finite element analysis method to achieve this goal. Based on the analysis results, burst speeds are calculated using various fracture criteria. When the calculations are done, impeller geometries are manufactured. Test geometries are named Geometry-1 and Geometry-2. Visuals and cross-sections of parts are shared in Figure 1.8 - Figure 1.11. Parts are tested in a spin test rig, burst events are observed, and actual burst speeds are recorded. Finally, calculated burst speeds are compared with the actual burst speed.

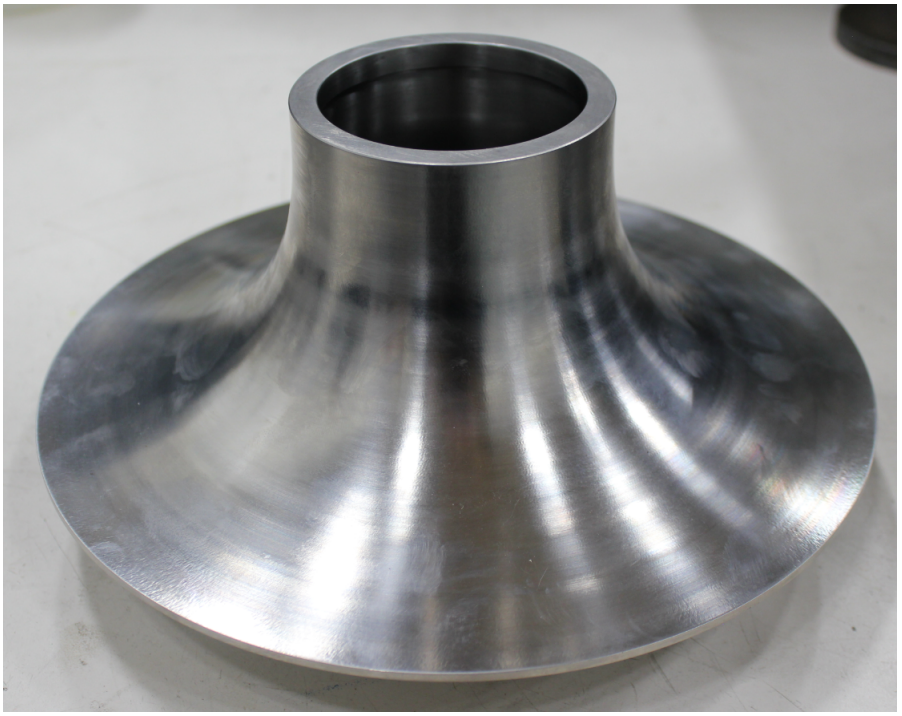

Figure 1.8 Manufactured Test Part, Geometry-1

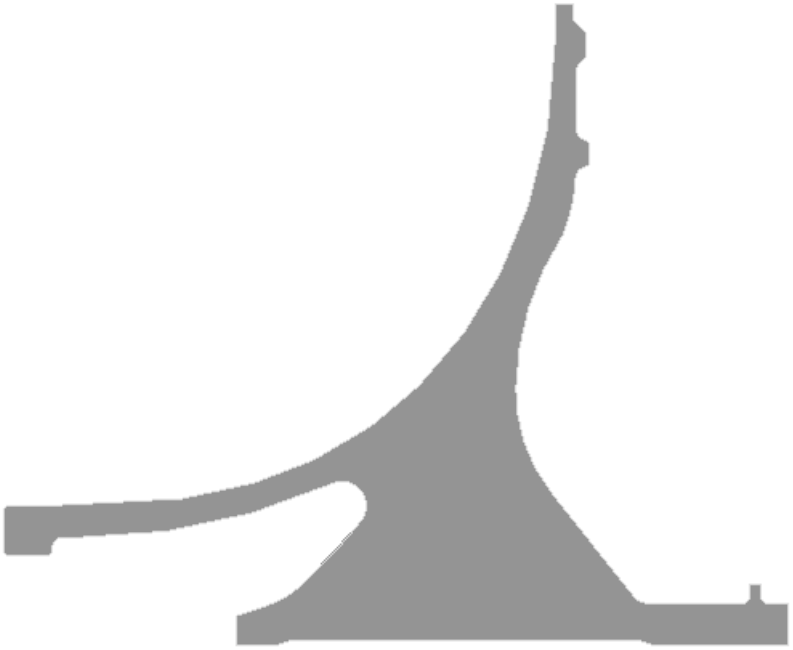

Figure 1.9 Cross-section of Geometry-1

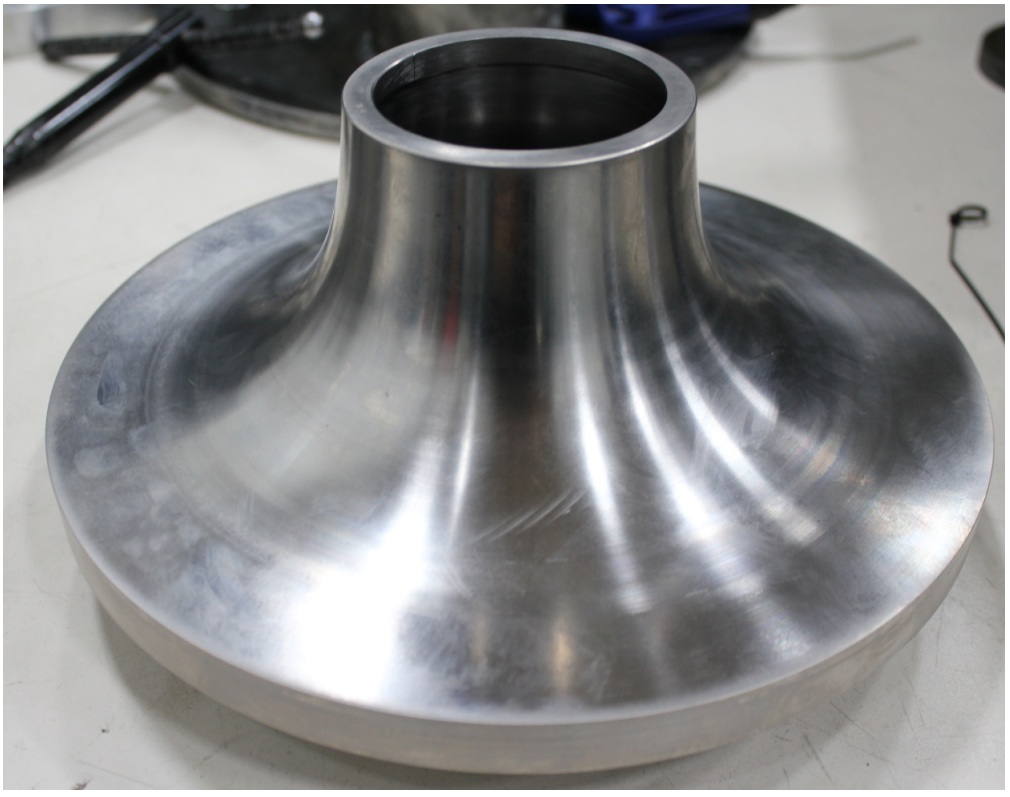

Figure 1.10 Manufactured Test Part, Geometry-2

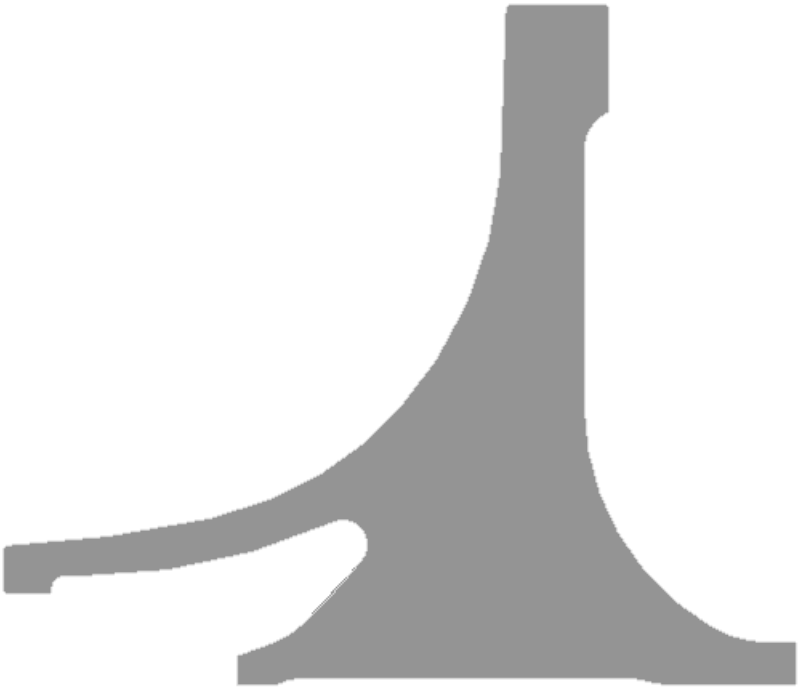

Figure 1.11 Cross-section of Geometry-2

2. THEORY

2.1. Material Behavior

Metallic materials can be classified into two main categories, brittle and ductile. Brittle materials generally fail after reaching the end of the elastic region. (Figure 2.1-c) The fracture occurs with small elastic deformation and negligible plastic deformation. Ductile materials are prone to plastically deform and show large deformation before fracture. (Figure 2.1-a) Beyond the yield point, some metallic materials start to show hardening behavior. (Figure 2.1-b)

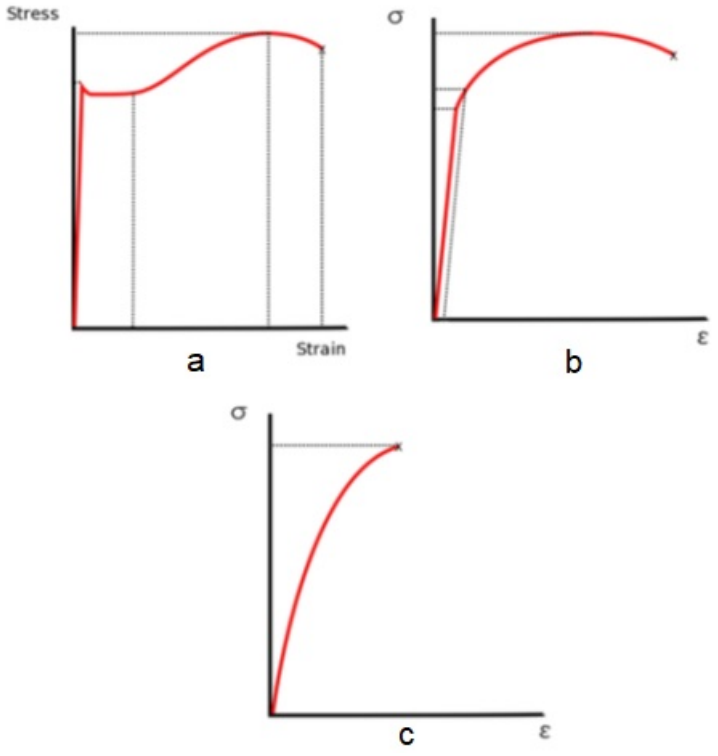

Figure 2.1 Material Behaviors

In this study, the impellers are made of Titanium-6Al-4V. Ti64 is a ductile material and shows strain hardening behavior.

2.1.1. Elastic Field

In the linear region, metallic material behavior can be defined by using Hooke's Law. This law was discovered by Robert Hooke in 1678, and the most simplified form of the law is given in (3).

$$\sigma = E\varepsilon \tag{3}$$

where ε is the strain, E is the modulus of elasticity, and the σ is the stress. The modulus of elasticity, also called Young's modulus, value differs from material to material, and the value depends on the material crystal structure, composition, and bonding type of atoms.

Modulus of elasticity can be found by performing a uni-axial tension test. In this test, the ratio of stress by strain gives the modulus of elasticity. Under uni-axial loading, if the tensile force is applied in the axial direction, the test specimen elongates axially and shrinks laterally, Poisson's ratio can be calculated by dividing lateral strain by axial strain.

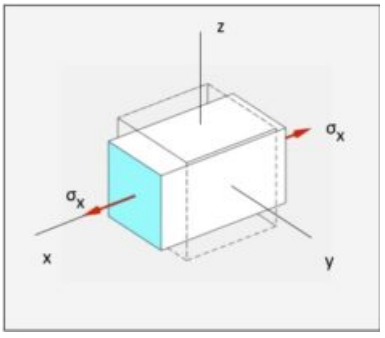

Figure 2.2 Poisson's Effect

$$v = \left|\frac{lateral strain}{axial strain}\right| = -\frac{e_y}{e_x} = -\frac{e_z}{e_x} \tag{4}$$

$$e_x = \frac{-v\sigma_y}{E} e_x = \frac{-v\sigma_z}{E} \tag{5}$$

$$e_x = \frac{\sigma_x}{E} \tag{6}$$

The general equation of Hooke's law can be shown as;

$$e_x = \left(\frac{1}{E}\right)[\sigma_x - v(\sigma_x + \sigma_z)] \tag{7}$$

Principal stresses are the normal stresses and act onto the principal planes that have zero shear stress. Principal stresses can be calculated using the following equation (8). The three roots of equation are the principal stresses σ_1, σ_2 and σ_3.

$$\sigma_p^3 - I_1\sigma_p^2 - I_2\sigma_p - I_3 = 0 \tag{8}$$

where

$$I_1 = \sigma_{yy} + \sigma_{yy} + \sigma_{zz} \tag{9}$$

$$I_2 = \sigma_{yz}^2 + \sigma_{zx}^2 + \sigma_{xy}^2 - \sigma_{yy}\sigma_{zz} - \sigma_{zz}\sigma_{xx} - \sigma_{xx}\sigma_{yy} \tag{10}$$

$$I_3 = \sigma_{xx}\sigma_{yy}\sigma_{zz} + 2\sigma_{yz}\sigma_{zx}\sigma_{xy} - \sigma_{xx}\sigma_{yz}^2 - \sigma_{yy}\sigma_{zx}^2 - \sigma_{zz}\sigma_{xy}^2 \tag{11}$$

Von-Mises stress yield criterion, also called the maximum distortion energy criterion, is a widely used yield criterion for ductile materials. This criterion states that if the Von-Mises stress value exceeds the material yield strength, the material starts to show plastic deformation. The Von-Mises stress can be calculated using principal stresses with the following equation.

$$\sigma_{vm} = \left[\frac{(\sigma_1 - \sigma_2)^2 + (\sigma_2 - \sigma_3)^2 + (\sigma_3 - \sigma_1)^2)}{2}\right]^{1/2} \tag{12}$$

2.1.2. Plastic Field

When a ductile metallic material exceeds the linear region, it starts to deform permanently, and this region is referred to as plastic region, see Figure 2.3. In the plastic region, the material deforms permanently and cannot return to its initial shape even if the external load is removed, and this effect is called plasticity.

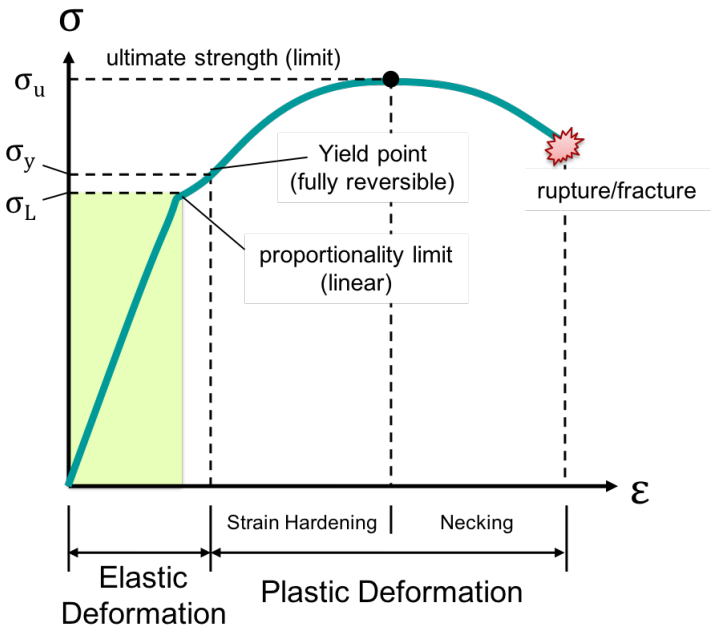

Figure 2.3 Stress-Strain Curve

Hardening behavior, also known as strain hardening or work hardening, causes a permanent change in the yield point. There are two hardening rules to define the hardening behavior of materials, isotropic hardening, and kinematic hardening. The isotropic hardening rule states that tensile and compressive yield points increase equally. The position of the yield surface does not change but equally increases in all directions. On the other hand, the kinematic hardening rule states that the size of the yield surface does not change but moves. (Figure 2.4)

In the plastic field, Hooke's law is not applicable to define material behavior and additional material models required. These models will be discussed in the following chapter

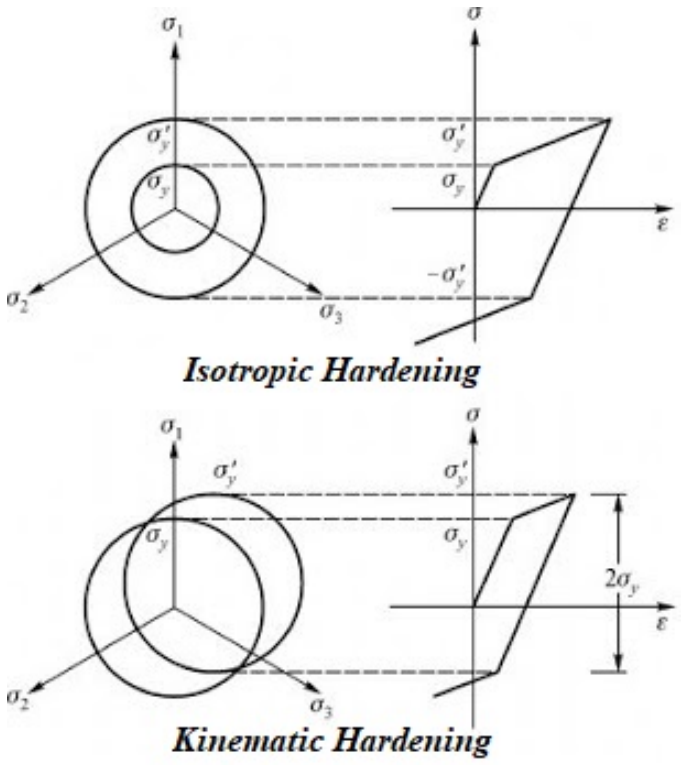

Figure 2.4 Isotropic and Kinematic Hardening

2.2. Material Models

Beyond the yield point, additional material models are required to define material behavior. In elastoplastic analyses, the non-linear relationship between strain and stress is defined with Ramberg-Osgood model. In explicit dynamic analyses, Johnson-Cook Material Model and Johnson-Cook Material Failure Model are used to define material plasticity and failure behaviors of material.

2.2.1. Ramberg-Osgood Material Model

W. Ramberg and W. Osgood proposed the Ramberg-Osgood material model in 1943 to describe the non-linear relationship between strain and stress. [11] This model defines the elastic region with a line and the plastic region with a power law. In the Ramberg-Osgood

equation, K is the material non-linear modulus, ε is the strain, n is the material strain-hardening exponent, σ is the stress, and E is the Young's Modulus.

$$\varepsilon = \frac{\sigma}{E} + K\left(\frac{\sigma}{E}\right)^n \tag{13}$$

The Ramberg-Osgood equation can be written in a more convenient way using yield strength term, σ_y, and it becomes:

$$\varepsilon = \frac{\sigma}{E} + \alpha\left(\frac{\sigma_y}{E}\right)\left(\frac{\sigma}{\sigma_y}\right)^n \tag{14}$$

In equation 14 α equals $K\left(\frac{\sigma_y}{E}\right)^{(n-1)}$. $\alpha\left(\frac{\sigma_y}{E}\right)$ term can be seen as a yield offset and be considered equal to 0.2% yield offset, which is applicable to most metal materials. (Figure 2.5)

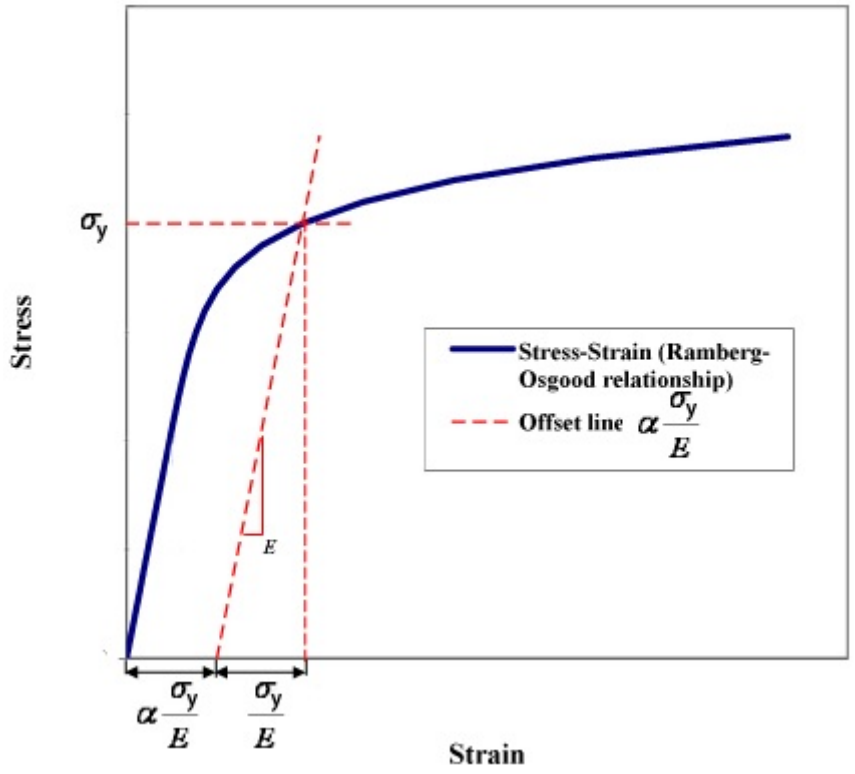

Figure 2.5 Ramberg-Osgood Equation Offset Line

2.2.2. Johnson-Cook Material Model

Johnson-Cook material model is one of the most often used empirical material model to define material behavior under high temperatures, high strain rates, and large strains. The model was proposed by Gordon Johnson and William Cook in 1983. [12] In the literature, this material model is widely used to define isotropic materials, and it is compatible with 2D and 3D finite element analysis element types.

$$\sigma = [A + B\varepsilon^{n}][1 + Cln\dot{\varepsilon}^{*}][1 - T^{*m}] \tag{15}$$

$$T^{*m} = \frac{(T - T_{room})}{(T_m - T_{room})} \tag{16}$$

$$\dot{\varepsilon}^{*} = \frac{\dot{\varepsilon}}{\dot{\varepsilon}_0} \tag{17}$$

In the Johnson-Cook material model; A is the yield strength of the material, C is the strain rate coefficient, B is the strain hardening constant, n is the strain hardening coefficient, T is the deformation temperature, T^{*m} is the homologous temperature, T_m is the material melting point, T_r is the reference temperature, $\dot{\varepsilon}_0$ is the reference strain rate, $\dot{\varepsilon}^{**}$ and $\dot{\varepsilon}$ are the strain rates and m is the thermal softening coefficient, .

2.2.3. Johnson-Cook Material Model

Failure of ductile material under large strain rates, temperature, and pressure loads can be defined using the Johnson-Cook material failure model. The model implies that damage builds up in the material during plastic straining and accelerates as soon as it reaches a critical value. The dynamic fracture strain equation proposed by Gordon Johnson and William Cook has shown in (18). [13]

$$\varepsilon_f = [D_1 + D_2 e^{D_3 \sigma^{*}}][1 + D_4 ln(\dot{\varepsilon}^{*})][1 + D_5 T^{*}] \tag{18}$$

Where D_1, D_2, D_3, D_4 and D_5 are the material constants, σ_{eq} is the equivalent von mises stress, σ_m is the mean stress, T^* is the homologous temperature, $\dot{\varepsilon}^*$ is the strain rate, and σ^* is the multiplication of σ_m and σ_{eq}.

2.3. Experimental Tensile Tests

There are different methods to obtain a stress-strain curve of materials, such as tensile, compression, torsional, and shear test. The tensile test is one of the most common methods because it can be easily performed compared to other methods. Using stress-strain curve, essential material properties such as ultimate tensile strength, Young's modulus, yield strength, hardening and softening phase can be obtained.

In the tensile test, a gradually increasing tensile load applies along the long axis of a specimen, and the applied load and elongation are measured continuously. Engineering stress and strain on the specimen can be calculated using measured data. [14]

$$\sigma = \frac{F}{A_0} \tag{19}$$

where F is the applied force, σ is the engineering stress and A_0 is the original cross-sectional area of specimen.

$$\varepsilon = \frac{l_i - l_0}{l_0} = \frac{\Delta l}{l_0} \tag{20}$$

where l_i is the instantaneous length, l_0 is the original length and ε is the engineering strain.

When calculating engineering stress, just the original cross-sectional area is taken into account, but in reality, there is a reduction in the cross-sectional area due to necking, and sometimes it is more meaningful to use true stress and strain values. The difference between true and engineering stress-strain curves can be seen in Figure 2.6.

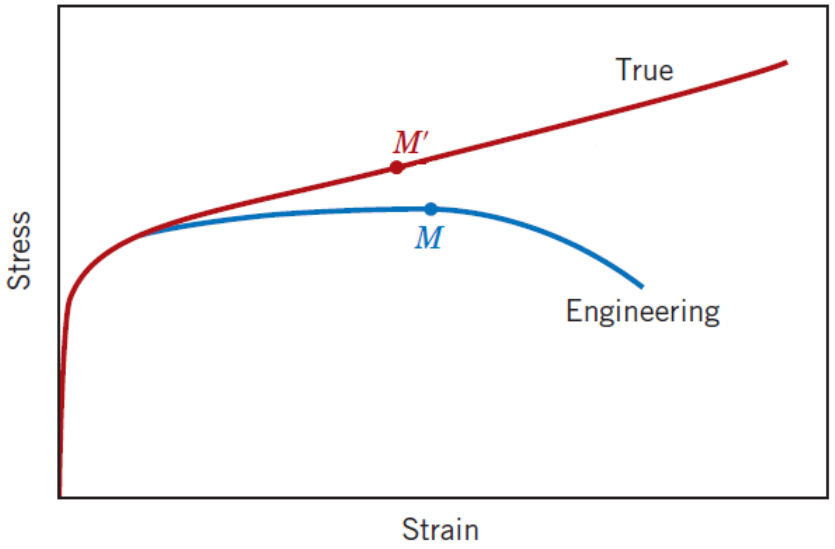

Figure 2.6 Engineering and True Stress-Strain Curves

[14]

$$\sigma_T = \frac{F}{A_i} = \sigma(1+\varepsilon) \tag{21}$$

where F is the applied force, A_i is the instantaneous cross-sectional area of specimen and σ_T is the true stress.

$$\varepsilon_T = ln\frac{l_i}{l_0} = ln(1+\varepsilon) \tag{22}$$

where l_o is the original length, l_i is the instantaneous length, and ε_T is the true strain.

2.4. Finite Element Analysis

2.4.1. Brief History of FEM and Preferred Software

In the 1940s first numerical methods started to develop. Richard Courant proposed to break a continuous system into subdomains. In the 1950s, analog computers developed, and more

complex problems, like matrix-based solutions of truss and frame structures, could be solved. For example, Boeing modeled airplane wing using triangular stress elements. In 1960, Clough stated "Finite Element" term first time. In the 1970s, FEM matured enough to use in different areas such as aviation, medicine, electricity, construction, machinery, etc., and it is still widely used today. [15]

In this thesis, ANSYS Workbench is used as an FE solver and modeling tool. ANSYS Workbench is a widely used software in academia and industry and can be considered a stable and reliable platform.

2.4.2. Finite Element Analysis Theory

The Finite Element Method is extensively used in industry and academic fields to solve complex problems. Partial differential equations that are too complex to be solved analytically can be solved with the high computational power of computers.

In the FEM, large and complex domains are subdivided into small elements that are easy to solve. It starts to solve a problem with a local stiffness matrix which is defined on each element, then continues with a global stiffness matrix by assembling elemental matrices, and lastly, solves the whole system.

The main advantage of FEM is that it can solve any system regardless of complexity by discretization the system into smaller elements, but this method also creates a disadvantage. In this approach, the real problem turns into an algebraic system and obtains solutions only for nodes. To obtain values rest of the element calculates the mean values of nodes. Increasing the node number in the analysis increases solution accuracy but, on the other hand, increases solution time. Hence, selecting the correct mesh size is an important task to have an accurate solution and reasonable computing time.

Matrix notation of linear static analysis is shown in (2.19). In this equation Global Stiffness Matrix is denoted as K, Vector of Unknowns is denoted as U, and Force Vector is represented as F. This approach requires only one pass through the matrix equation solver and is only valid for small deflection theory.

$$Ku = F \tag{23}$$

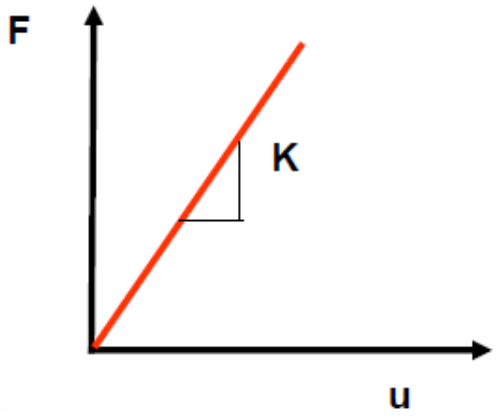

Figure 2.7 Linear Static Analysis Approach

[16]

Large deflection causes geometrical nonlinearity. In large deflection approach governing equation update incrementally. This process can be considered as diving the problem into many linear steps, and as the geometry deforms stiffness matrix is updated. [17]

$$Ku\Delta u = \Delta P \tag{24}$$

$$\Delta u = IncrementalDisplacementVector(Unknown) \tag{25}$$

$$\Delta P = IncrementalAppliedLoadVector(Known) \tag{26}$$

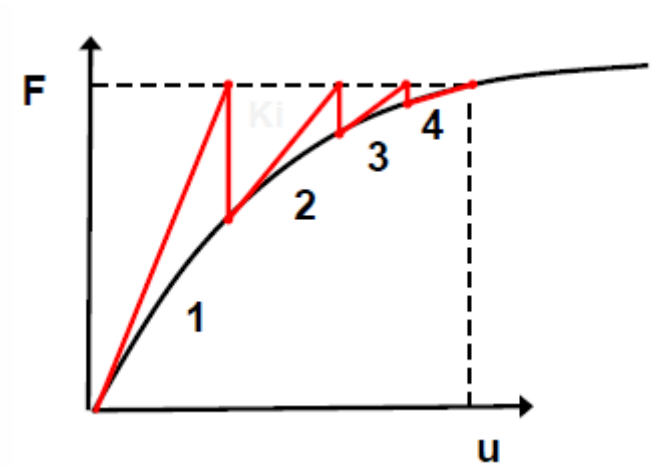

Figure 2.8 Non-linear Static Analysis Approach

[16]

In the ANSYS, if the *Large Deflection* is set to *On* under *Analysis Setting* problem will be solved using the large deflection approach; otherwise small deflection approach will be used. In this study, both small and large deflection approaches are used.

2.5. Explicit Dynamic Analysis Theory

Explicit dynamic analysis method is frequently used to simulate time-varying dynamic phenomena like explosion, drop and blast. Burst failure is a result of high deformation that occurs in a small-time step, and therefore using the explicit dynamic analysis method is suitable for this problem.

There are different methods to solve explicit problems. ANSYS explicit solver uses Lagrangian method. [18] In this method, firstly, forces acting on nodes calculate, and then computed force values diving by mass to obtain nodal accelerations.

$$\ddot{x}_i = \left(\frac{F_i}{m}\right) + b_i \tag{27}$$

where m is the mass of the node, $\ddot{x}_i$ is the nodal acceleration, b_i is the components of body acceleration, and F_i is the forces acting on the nodes.

After the nodal acceleration values obtained at time n, nodal velocity values can be found with:

$$\dot{x_i}^{n+1/2} = \dot{x_i}^{n-1/2} + \ddot{x_i}^{n} \Delta t^{n} \tag{28}$$

Lastly, nodal positions at the time n+1 were obtained by integrating velocities:

$$\dot{x_i}^{n+1} = \dot{x_i}^{n} + \ddot{x_i}^{n+1/2} \Delta t^{(n+1)/2} \tag{29}$$

In the Lagrangian method, the material model and mesh move and distort together; hence mass conservation satisfies automatically. Density can be calculated from the initial mass of the zone and its current volume. (30)

$$\frac{\rho_0 \nu_0}{\rho} = \frac{m}{\rho} \tag{30}$$

Momentum conservation equations linked with stress tensor σ_{ij} shared below.

$$\rho \ddot{x} = b_x + \frac{\partial \sigma_{xx}}{\partial_x} + \frac{\partial \sigma_{xy}}{\partial_y} + \frac{\partial \sigma_{xz}}{\partial_z} \tag{31}$$

$$\rho \ddot{y} = b_y + \frac{\partial \sigma_{yx}}{\partial_x} + \frac{\partial \sigma_{yy}}{\partial_y} + \frac{\partial \sigma_{yz}}{\partial_z} \tag{32}$$

$$\rho \ddot{y} = b_z + \frac{\partial \sigma_{zx}}{\partial_x} + \frac{\partial \sigma_{zy}}{\partial_y} + \frac{\partial \sigma_{zz}}{\partial_z} \tag{33}$$

The energy conservation equation is shared below.

$$\dot{e} = \frac{1}{\rho} + (\sigma_{xx}\dot{\varepsilon}_{xx} + \sigma_{yy}\dot{\varepsilon}_{yy} + \sigma_{zz}\dot{\varepsilon}_{zz} + \sigma_{xy}\dot{\varepsilon}_{xy} + \sigma_{yz}\dot{\varepsilon}_{yz} + \sigma_{zx}\dot{\varepsilon}_{zx}) \tag{34}$$

2.6. Fracture Criteria

There are several criteria to determine the possible rotational speed that burst failure occurs. In this thesis, Radial Stress Criterion, Robinson's Criteria, and Inertial Instability Criterion (Critical Strain Criteria) are used.

2.6.1. Robinson's Criteria

Robinson Criteria is a widely used criterion in the aerospace industry as a rule of thumb was proposed by Robinson in 1944. [19] It is required to have ultimate engineering tensile strength and mean hoop stress values.

$$\omega_{burst} = \omega \sqrt{\frac{\sigma_{UTS}}{\sigma_{c,mean}}} \tag{35}$$

2.6.2. Critical Strain Through Cross-section Criteria

Critical strain through cross-section criteria proposed by Y.A. Nozhnitsky and A.N. Servetnik [20] implies that burst failure occurs if the plastic strain is reached through any cross-section of the disc. In equation 2.28, ε is the engineering strain, ε_c^p is the critical plastic strain, and σ_{UTS} is the ultimate engineering tensile stress.

$$\varepsilon_c^p = \ln\left(1 + \varepsilon(\sigma_{UTS})\right) - \frac{\sigma_{UTS}(1 + (\varepsilon_{UTS}))}{E} \tag{36}$$

To include plasticity effects in the FEA material hardening model is defined, and the *Large Deflection* option is enabled.

2.6.3. Explicit Dynamic Analysis Criterion

The explicit dynamic analysis criterion aims to observe a fully developed crack on the disc. The rotational speed is increased to reach a fully developed crack to obtain detailed information about crack initiation location and crack propagation behavior.

3. METHODOLOGY

This chapter presents the workflow of the study.

3.1. Material Data

Impellers are made of pancake-shaped Ti64 forging material. Ti64 is a widely used material in the aerospace industry on account of its low density, high strength and excellent resistance against corrosion.

3.1.1. Experimental Tensile Tests

To obtain the exact material properties of Impellers, tensile test specimens are cut out from the same forging used in Impeller manufacturing. Four tensile test specimens, evenly spaced along the circumferential direction, are taken from both forgings and machined per ASTM E8 [21] standard. Tensile tests are performed under 300 °C uniform temperature per ASTM E21 [22] standard, and the stress-strain curve is created using the average material properties taken from specimens. The true stress-strain curves of Geometry-1 and Geometry-2 are normalized for 200 MPa and shared in Figure 3.2 and Figure 3.3. Obtained material data is used in finite element analyses.

Figure 3.1 Test Specimen Before and After Tensile Test

[23]

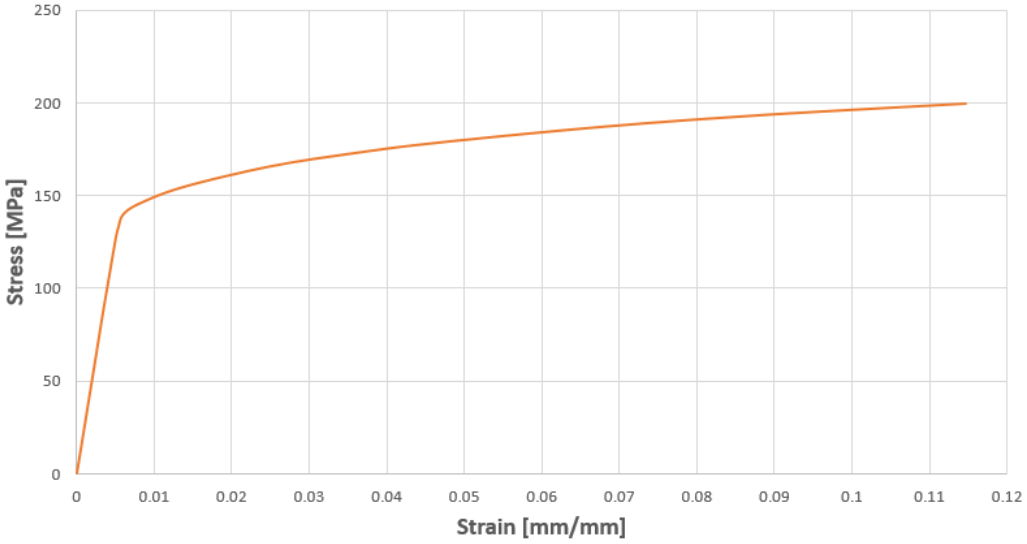

Figure 3.2 True Stress – Strain Curve of Geometry-1 [Normalized]

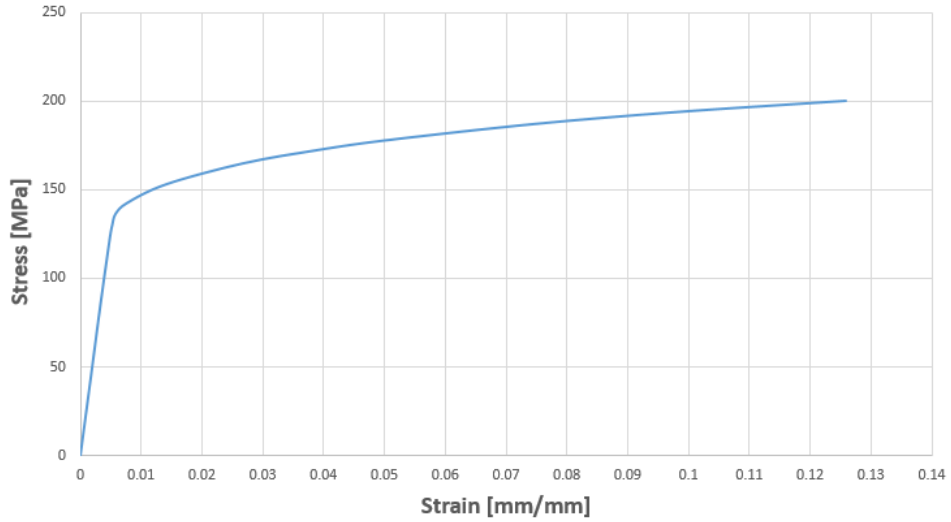

Figure 3.3 True Stress – Strain Curve of Geometry-2 [Normalized]

3.1.2. Johnson-Cook Material Model Parameters

Parameters of the Johnson-Cook material model are taken from a similar study [24] and shared in Table 3.1.

Parameter	A [MPa]	B [MPa]	C	n	m	$\dot{\varepsilon}_0$ $[s^{-1}]$
Value	862.5	331.2	0.012	0.34	0.8	1

Table 3.1 Constants of the Material Model for Ti64

3.1.3. Johnson-Cook Failure Model Parameters

Table 3.2 shows Johnson-Cook failure model parameters for Ti64, which are taken from another study. [25]

Parameter	D_1	D_2	D_3	D_4	D_5	T_{melt} $[°C]$
Value	-0.09	0.27	0.48	0.014	3.87	1640

Table 3.2 Constants of the Damage Law for Ti64

3.2. Preprocessing Model

All structural analyses are performed using ANSYS Mechanical 20.2. The 2D axisymmetric model is used in elastic and elastoplastic analyses to reduce the computing time, and the 3D full model is used in explicit dynamic analysis. Plane183 elements are used in 2D elastic and elastoplastic analyses, and Solid164 elements in 3D explicit dynamic analysis. In all of these analyses average element quality is targeted as 0.8.

3.2.1. Definition of PLANE183

Plane183 is a 2D, 8 or 6 node higher order element. It is suited to modeling irregular meshes with the help of quadratic displacement behavior. The description in the ANSYS manual is "*The element is defined by six or eight nodes having two degrees of freedom at each node: translations in the nodal x, and y directions. The element has plasticity, hyperelasticity, creep, stress stiffening, large deflection, and large strain capabilities. It also has mixed formulation capability for simulating deformations of nearly incompres.*" [26]

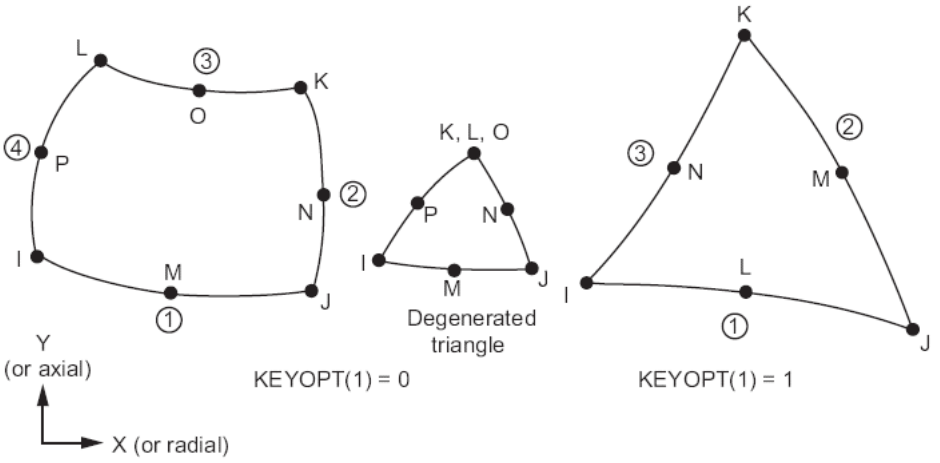

Figure 3.4 Geometry properties of PLANE183

3.2.2. Definition of PLANE164

Plane164 is a 3D, 8 node solid element that can only be used in explicit dynamic analysis and shown in 3.5 [26]. Each node of this element has freedom in the x, y, and z direction of acceleration, velocity, and translation. In addition, this element supports all non-linear behaviors supported by ANSYS.

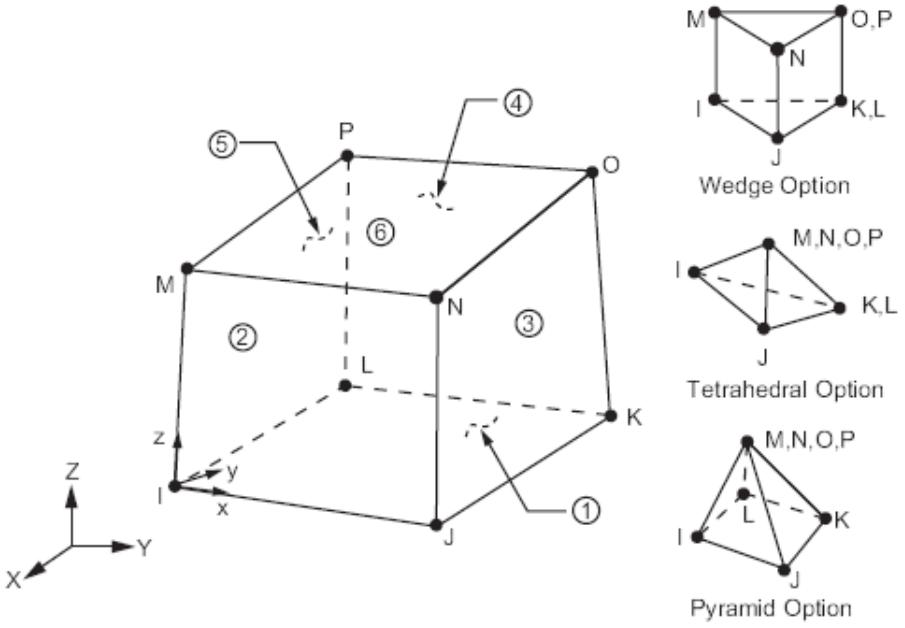

Figure 3.5 Geometry properties of SOLID164

3.3. Static Structural Analysis

Both elastic and elastoplastic analyses are performed using *ANSYS Workbench 20.2* Static Structural module. Boundary conditions of the geometry are shared in Figure 25, and the name of the specific regions in Figure 27. Displacement of parts tangentially and axially fixed and radially free. Under analysis settings, *Large Deflection* option is set to *On*, and *Nonlinear Effects* option is set to *Yes* due to expected large deformations. A uniform 300 °C temperature is applied, and *Thermal Strain Effects* is set to *No* to eliminate the effect of any temperature change.

3.3.1. Elastic Analysis

The rotational speed used in the elastic analysis is denoted as $\omega_{geo1}^{elastic}$ and $\omega_{geo2}^{elastic}$. *Isotropic Elasticity* and *Density* properties of Ti64 are defined under the *Engineering Data* section.

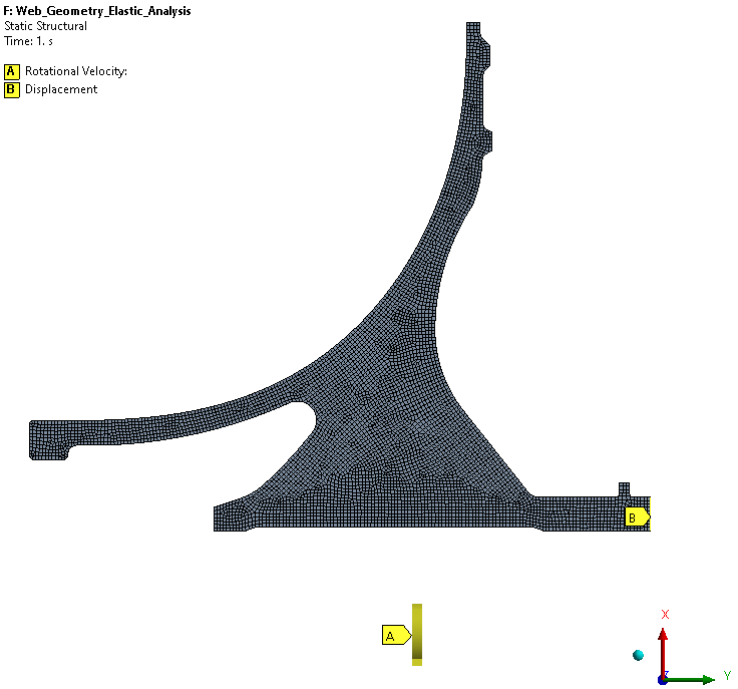

Figure 3.6 Elastic & Elastoplastic Analysis Mesh Detail and Boundary Conditions of Geometry-1

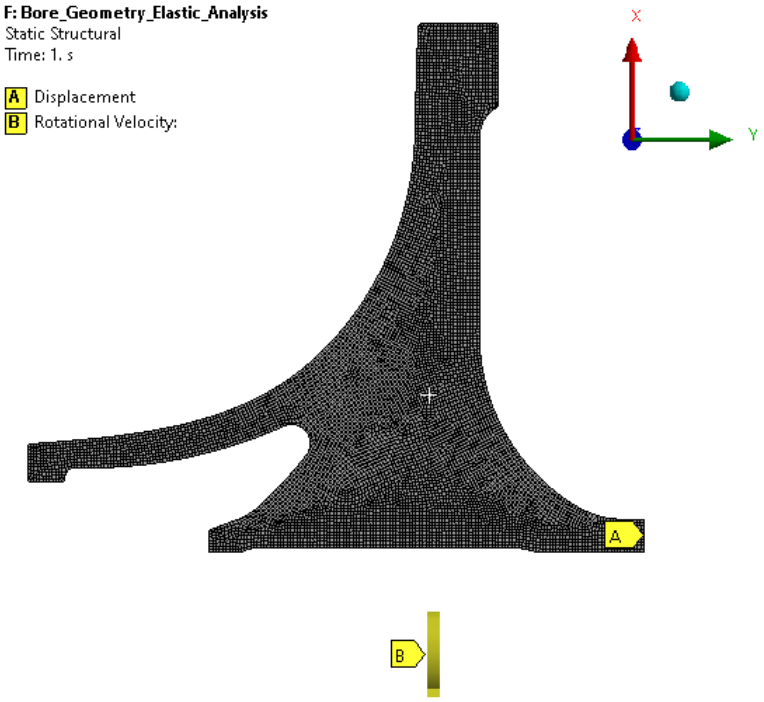

Figure 3.7 Elastic & Elastoplastic Analysis Mesh Detail and Boundary Conditions of Geometry-2

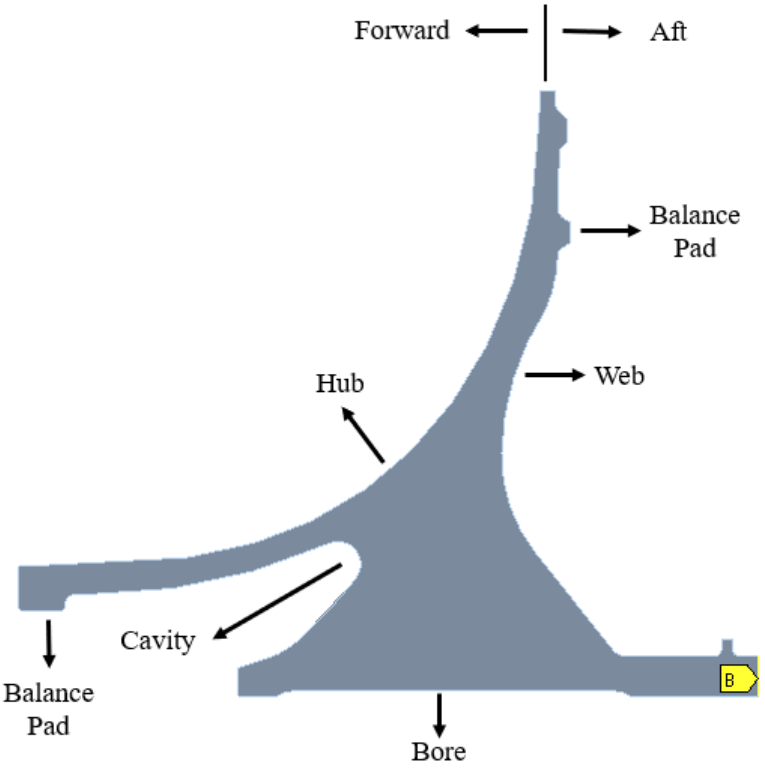

Figure 3.8 Specific Regions of Geometries

3.3.2. Elastoplastic Analysis

Material hardening data obtained from tensile tests are applied using the *Multilinear Kinematic Hardening* option under the *Engineering Data* section. The analysis is repeated until it reaches the non-convergence point, and the final speed is denoted as $\omega_{geo1}^{plastic}$ and $\omega_{geo2}^{plastic}$.

3.4. Explicit Dynamic Analysis

Johnson Cook Material and Material Failure Model are defined under the *Engineering Data* section. Material properties are shared in sections 3.1.2, and 3.1.3 are used. A uniform 300 °C temperature is applied. The displacement value is set to ”0” in the axial and radial directions. The rotational speed is increased until convergence is lost, and the final speed is denoted as $\omega_{geo1}^{explicit}$ and $\omega_{geo2}^{explicit}$. The analysis end time is set to 0.001. Boundary conditions and mesh details of the geometry are shared in Figure 28 and Figure 29, respectively.

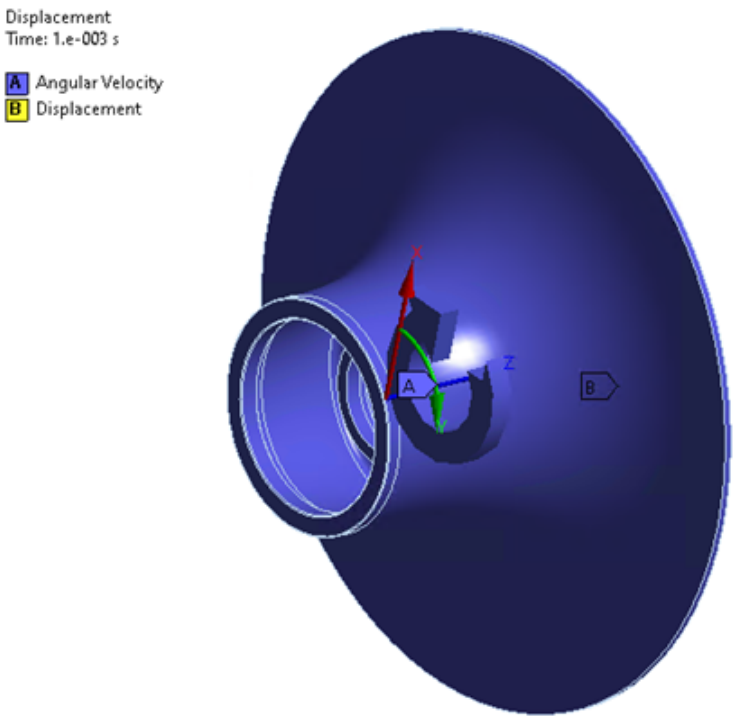

Figure 3.9 Explicit Dynamic Analysis Boundary Conditions of Geometry-1

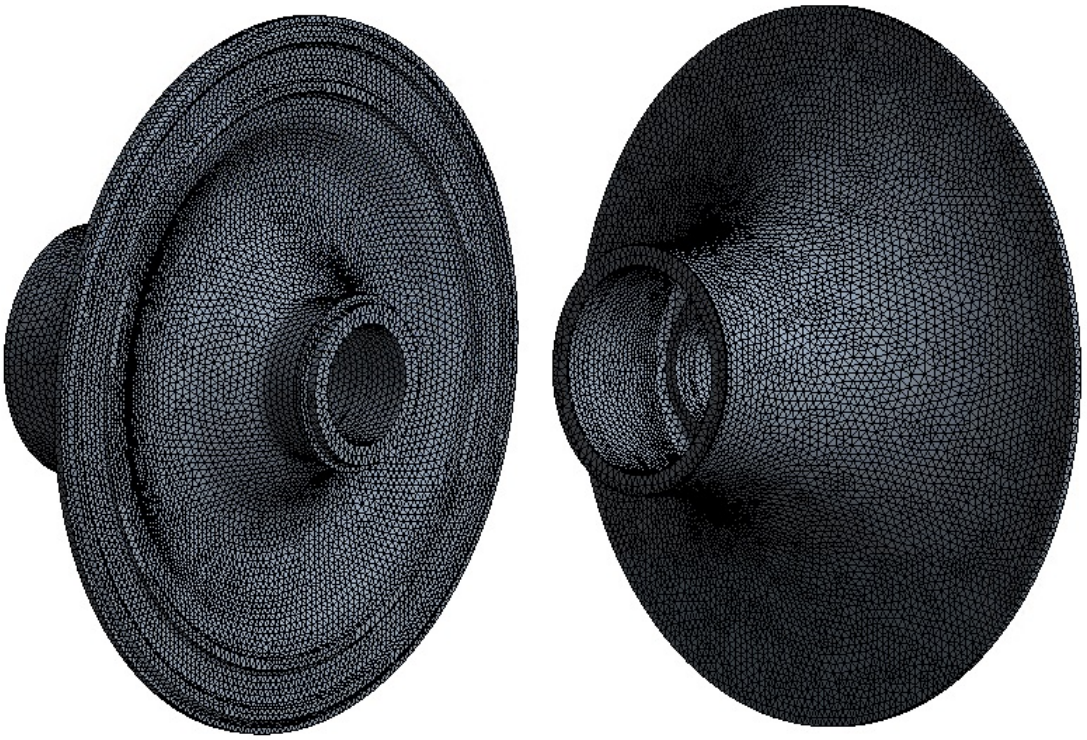

Figure 3.10 Explicit Dynamic Analysis Mesh Details of Geometry-1

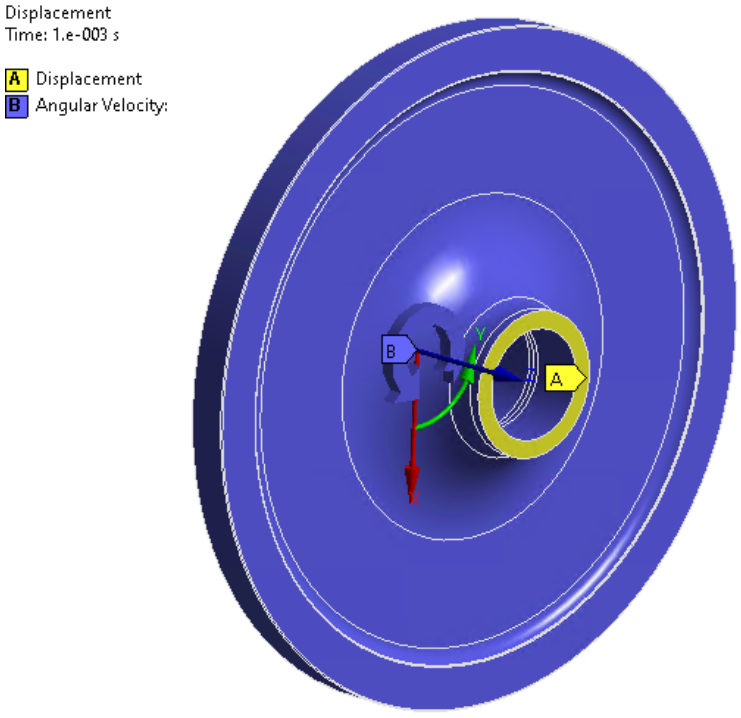

Figure 3.11 Explicit Dynamic Analysis Boundary Conditions of Geometry-2

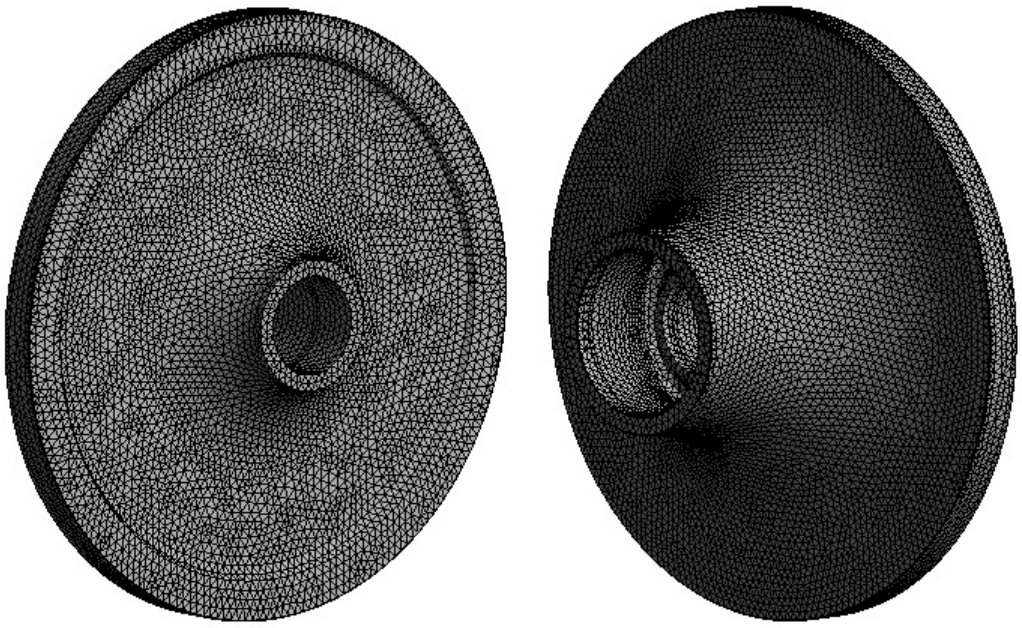

Figure 3.12 Explicit Dynamic Analysis Mesh Details of Geometry-2

3.5. Test Setup

Spin testing is a crucial step in ensuring the integrity and safety of high-speed rotor parts. Spin tests are generally performed in a test rig that is heavily armored to maintain protection against high-energy fragments and under vacuum conditions to eliminate air friction and the explosion risk of oil fog or metal dust. Two different drive systems are used to accelerate the rotor: high-speed electric motor and compressed air turbine.

In this study, the burst tests are performed under vacuum and uniform 300 °C temperature. A compressed air turbine drives the test rig. The rotational speed is increased until the burst event. The burst moment is recorded using a high-speed camera and the rotational speed of the part with a speed sensor. A schematic of the test rig is shared in Figure 3.13 [27]. Photos of the test part assembled on the test rig are shared in Figure 3.14 and Figure 3.15. An oven is used to heat the test parts assembled on the test rig, and a photo of it is shared in Figure 3.16. Recorded rotational speed profiles for Geometry-1 and Geometry-2 are shared in 3.17 and Figure 3.18, respectively.

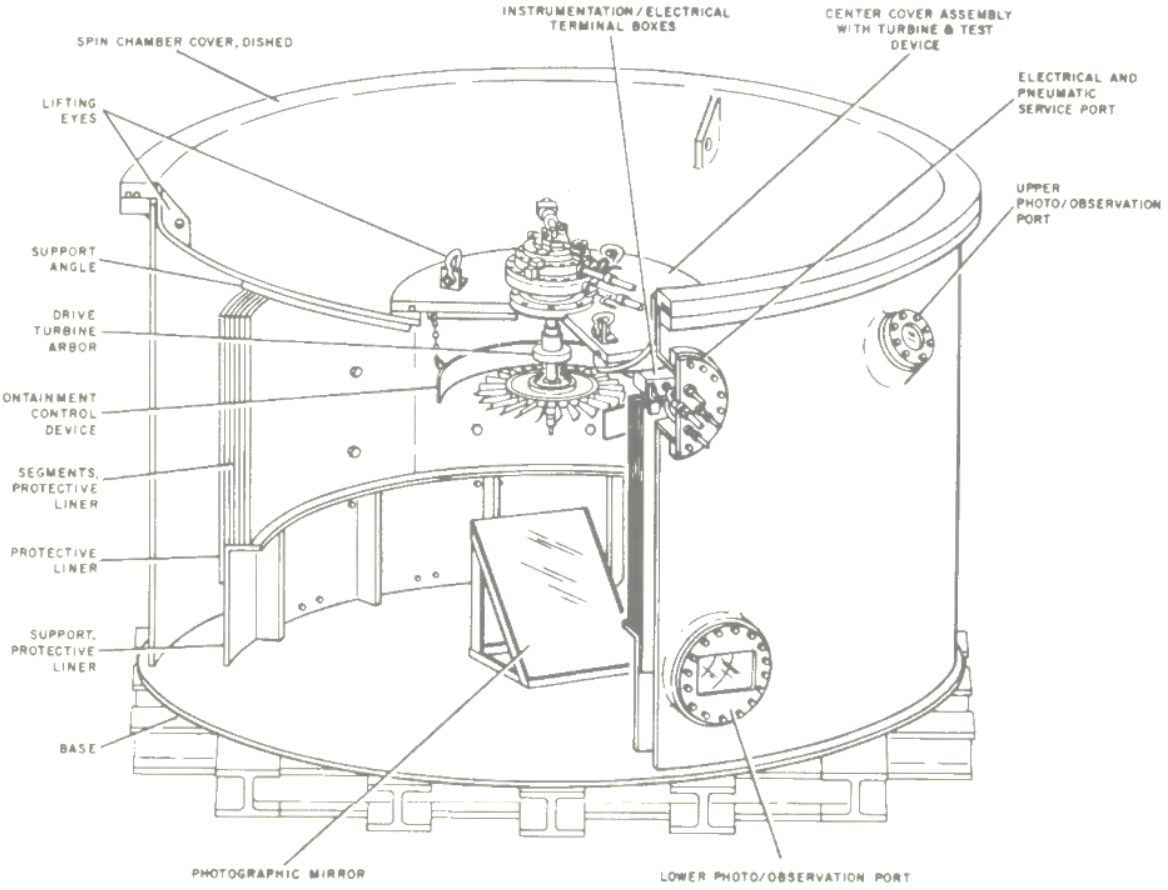

Figure 3.13 Spin Rig

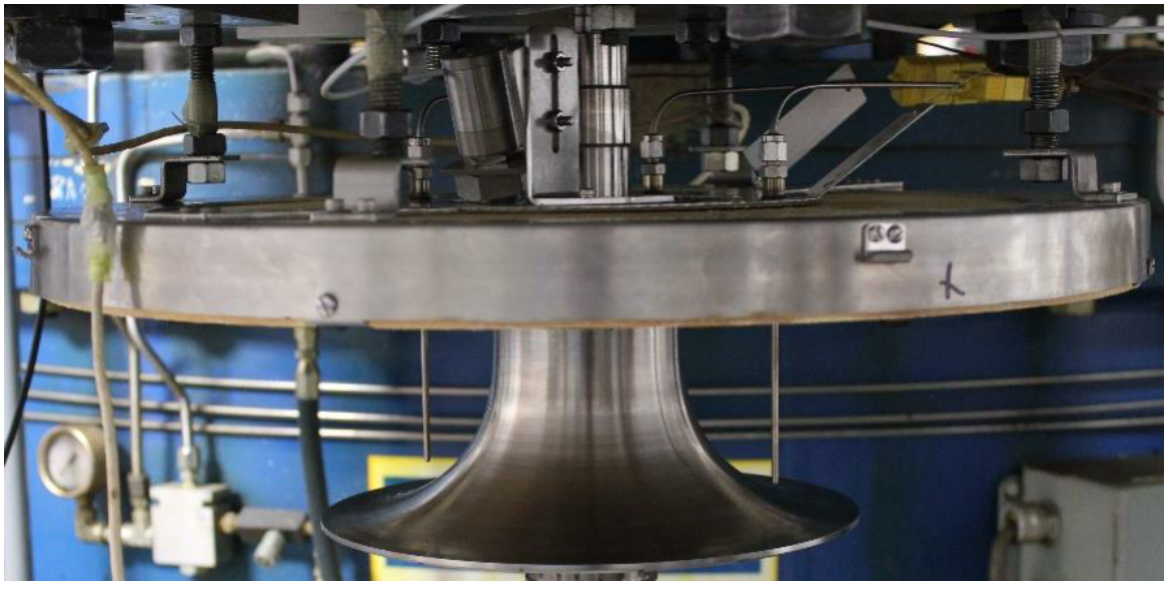

Figure 3.14 Geometry-1 Assembled on the Spin Rig

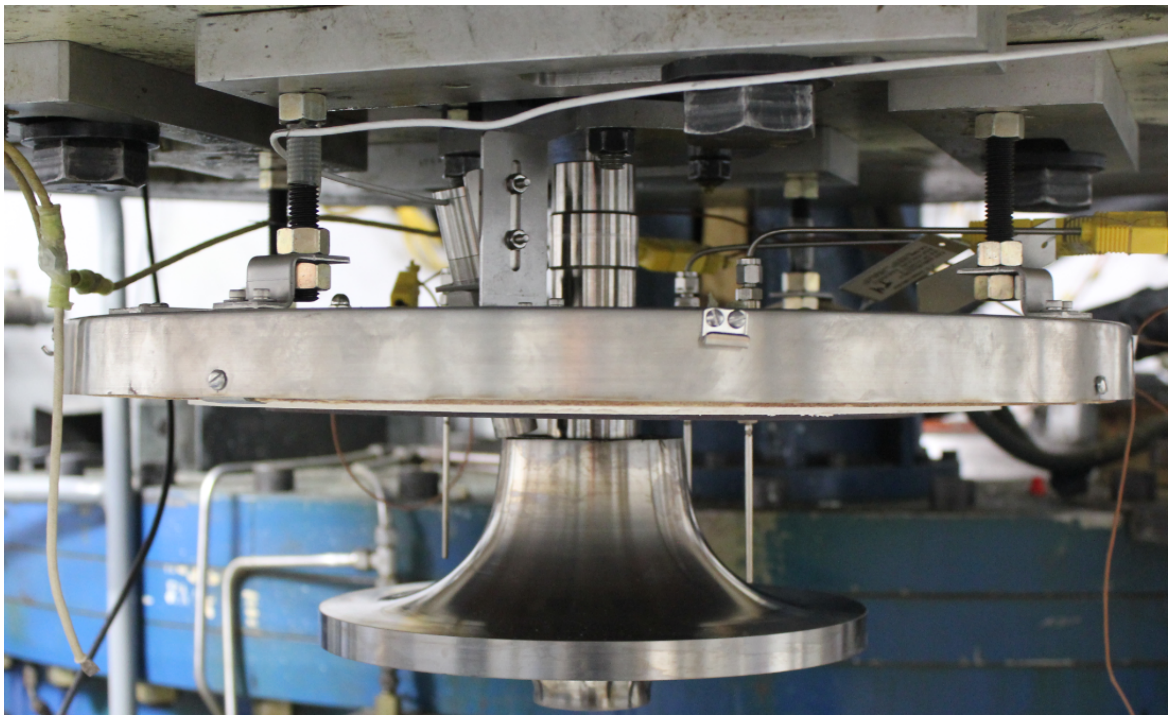

Figure 3.15 Geometry-2 Assembled on the Spin Rig

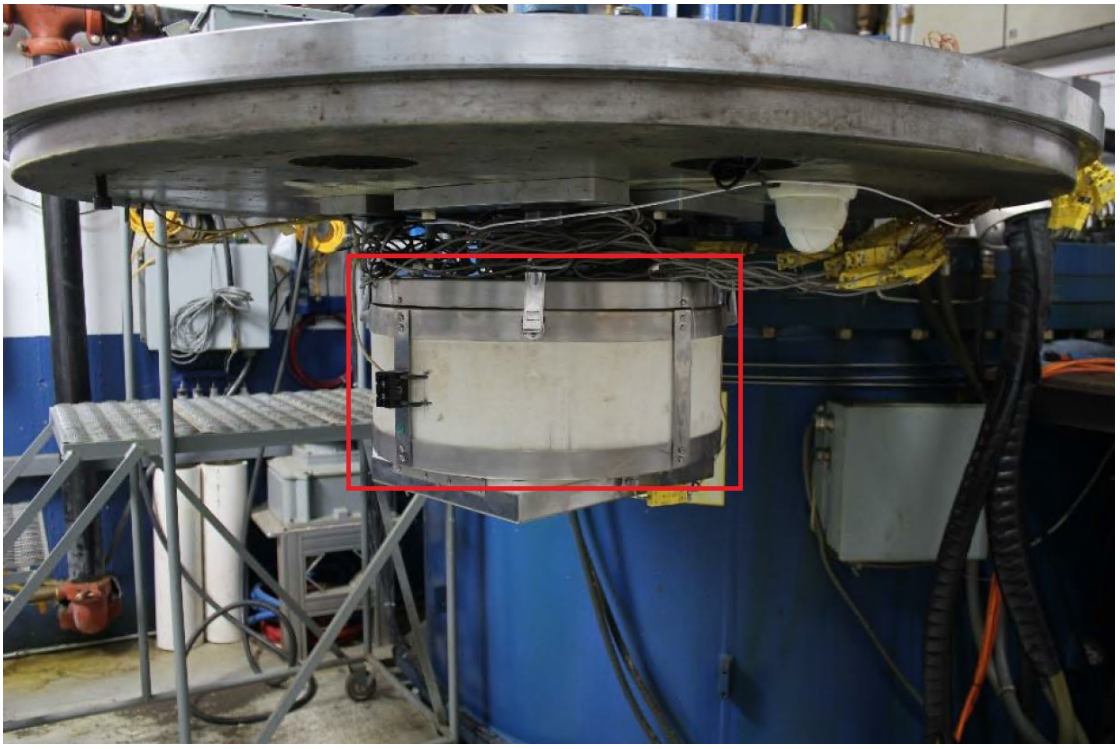

Figure 3.16 Oven Assembled on the Spin Rig

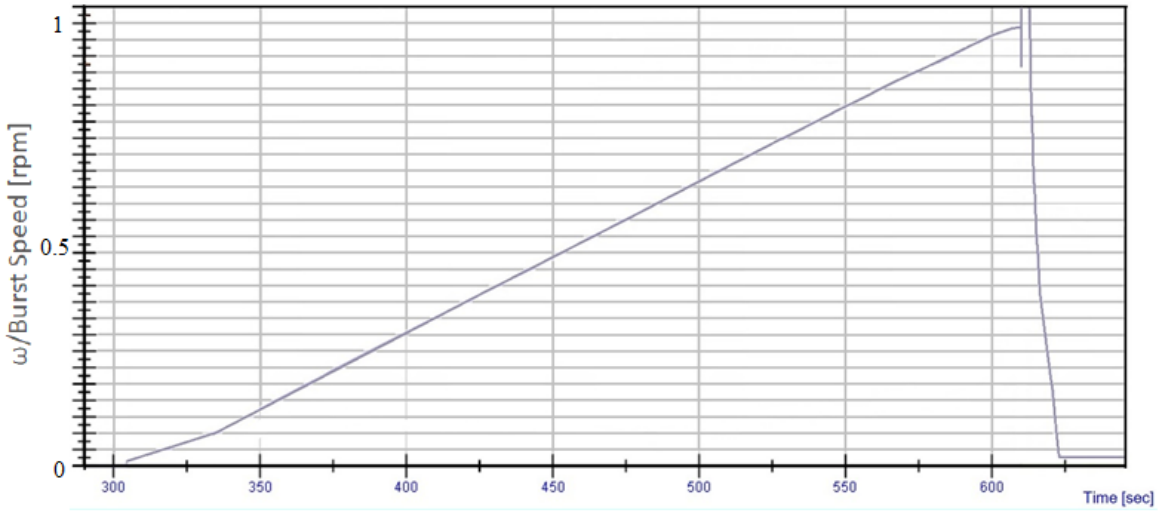

Figure 3.17 Speed Profile of Geometry-1

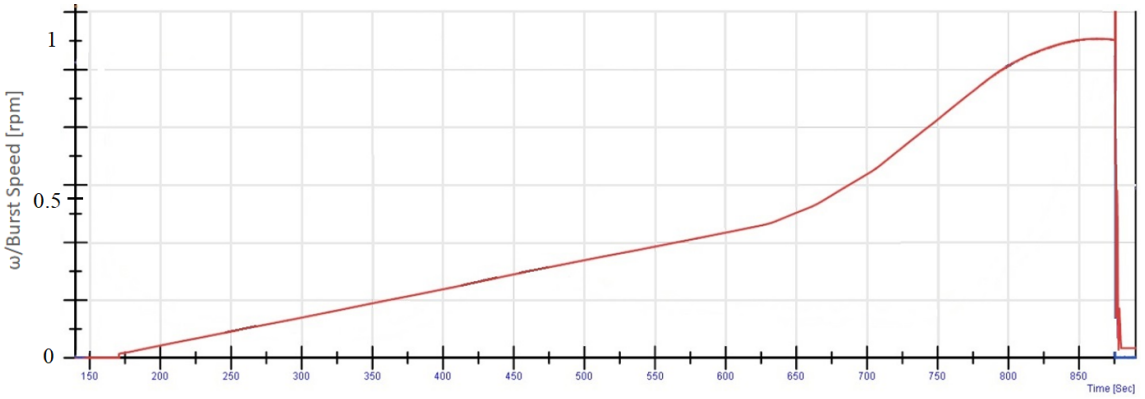

Figure 3.18 Speed Profile of Geometry-2

4. RESULTS

4.1. Numerical Results

This section shares the results of elastic, elastoplastic, and explicit analyses. Normalization is performed by dividing stress, strain, and deformation values by maximum stress, strain, and deformation values, respectively. There is no correlation between linear elastic, elastoplastic, and explicit analyses normalization values.

4.1.1. Results of Geometry-1

4.1.1.1. Elastic Analysis Results

Normalized stress, strain, and deformation plots are taken from elastic analysis with ω=$\omega_{geo1}^{elastic}$ shared in Figure 4.1-Figure 4.3. Radial stress is the highest stress component, and radial stress concentration has occurred in the middle of the web region. The tangential stress reaches 73.8% of the maximum radial stress, which occurred on the web region. Axial stress is the lowest stress component, and the axial stress concentration has occurred in the cavity region of the part.

Maximum total strain arises on the web region, and the outer diameter of the part is deformed forward direction.

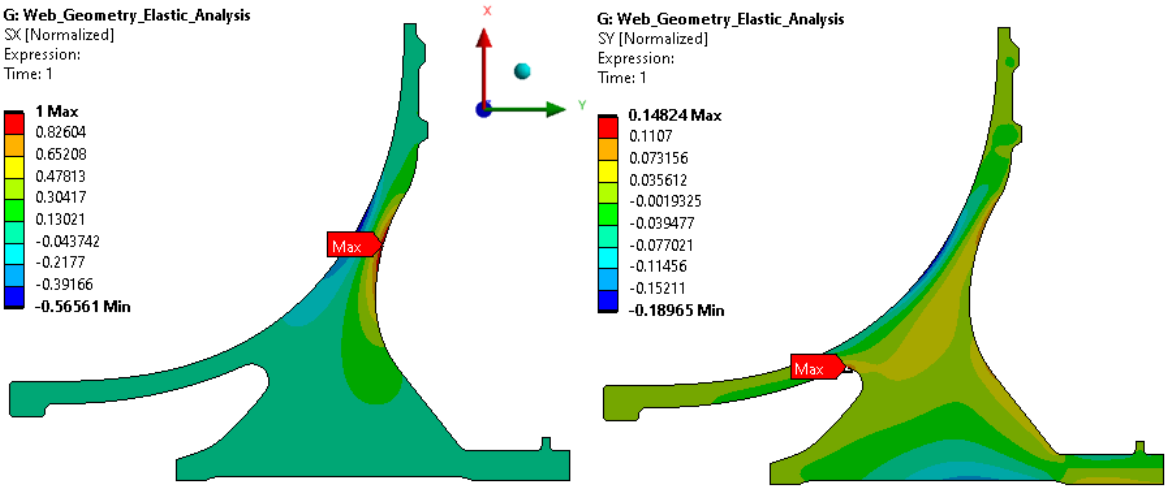

Figure 4.1 Normalized Radial and Axial Stress Plots from Elastic Analysis

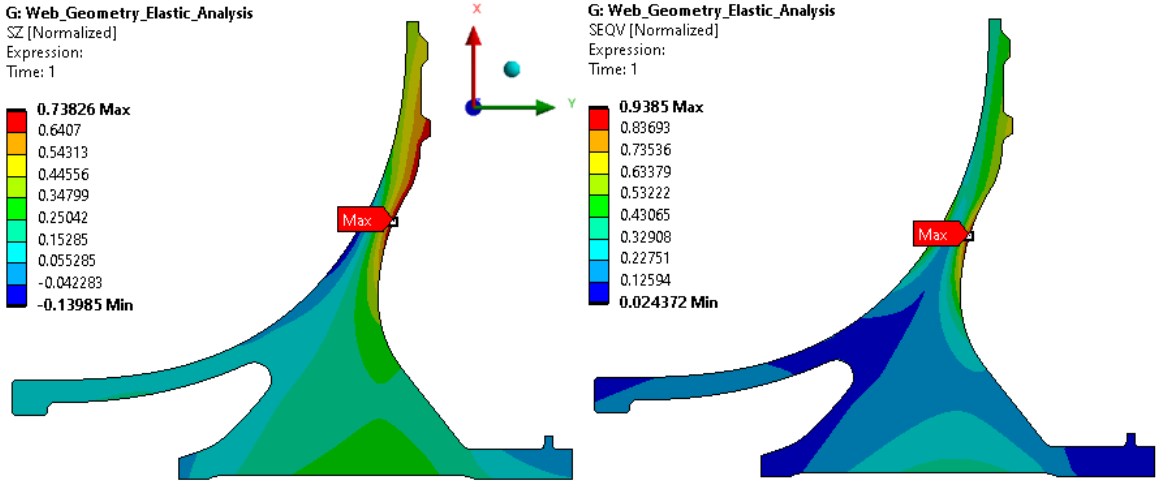

Figure 4.2 Normalized Tangential and Equivalent Stress Plots from Elastic Analysis

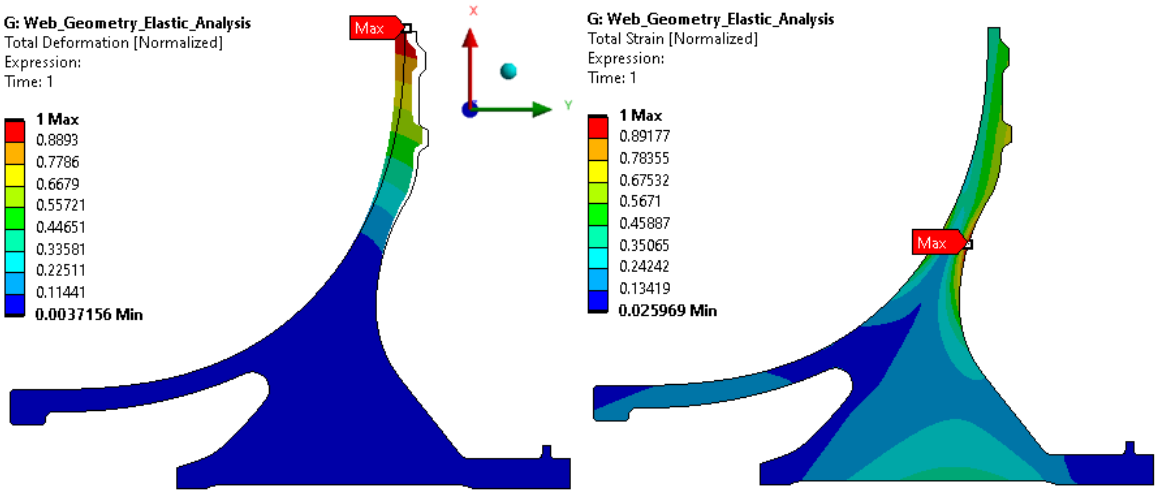

Figure 4.3 Normalized Total Deformation and Total Strain Plots from Elastic Analysis

4.1.1.2. Elastoplastic Analysis Results

Normalized stress, strain, and deformation plots from elastoplastic analysis with ω=$\omega_{geo1}^{plastic}$ are shared in Figure 41-Figure 43. Radial stress is the highest stress component, and radial stress concentration has occurred in the middle of the web region. The tangential stress reaches 96.7% of the maximum radial stress, and it has occurred inner section of the part below the web region. Axial stress is the lowest stress component, and the maximum value has occurred on the aft side of the bore, which seems reasonable given the boundary condition in Figure 3.6.

Maximum plastic strain arises on the web region, and the outer diameter of the part is largely deformed forward and radially elongated.

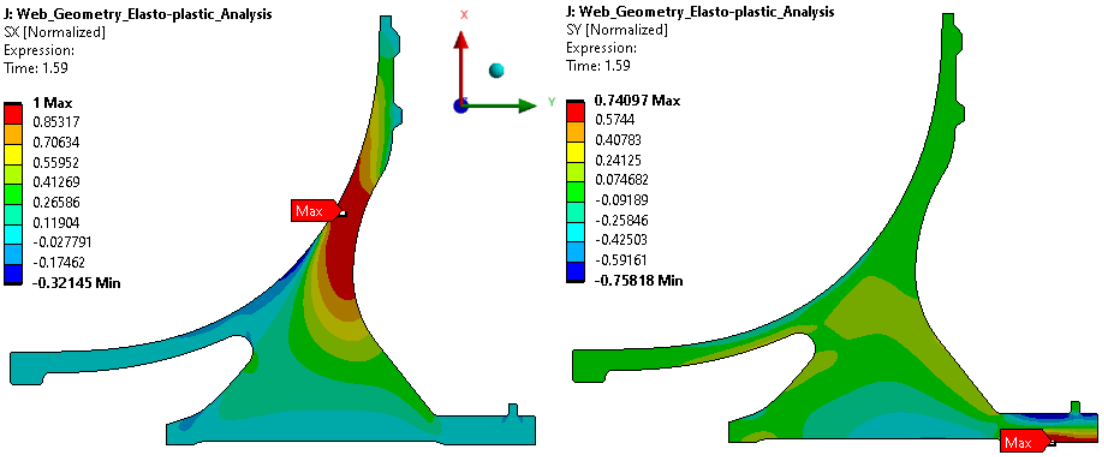

Figure 4.4 Normalized Radial and Axial Stress Plots from Elastoplastic Analysis

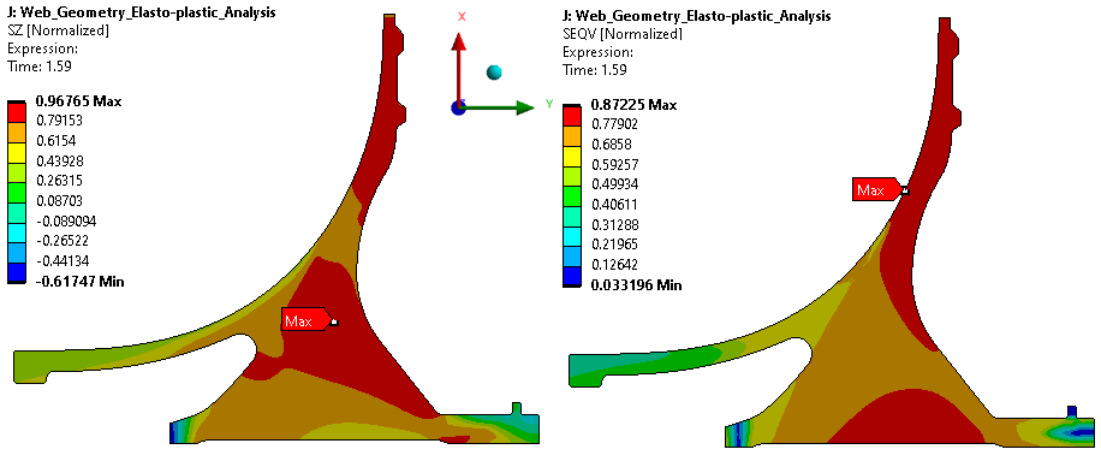

Figure 4.5 Normalized Tangential and Equivalent Stress Plots from Elastoplastic Analysis

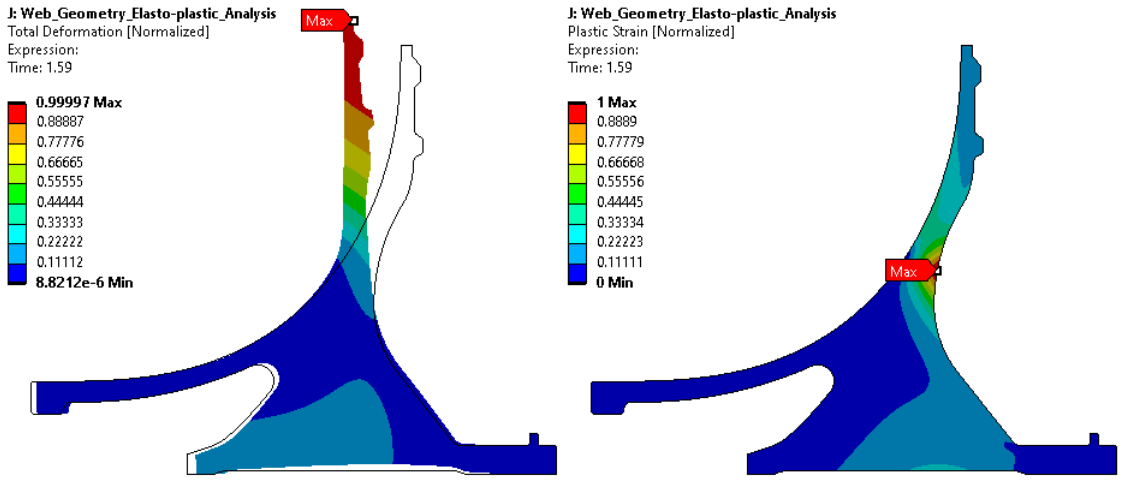

Figure 4.6 Normalized Total Deformation and Total Strain Plots from Elastic Analysis

4.1.1.3. Explicit Dynamic Analysis Results

Normalized equivalent stress and plastic strain plots are taken from explicit dynamic analysis with ω=$\omega_{geo1}^{explicit}$ shared in Figure 4.7-Figure 4.12. Crack initiation has occurred in the middle of the web region and propagated in the circumferential direction. The crack had initiated at the web location where the equivalent plastic stress has a maximum value.

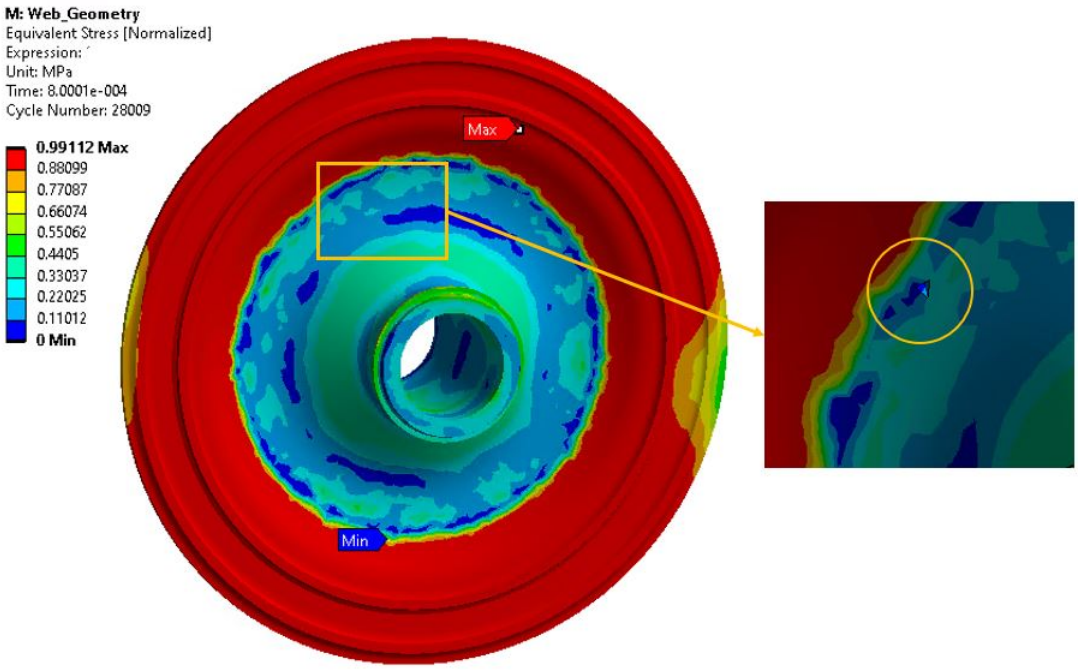

Figure 4.7 Normalized Equivalent Stress (Crack Initiation)

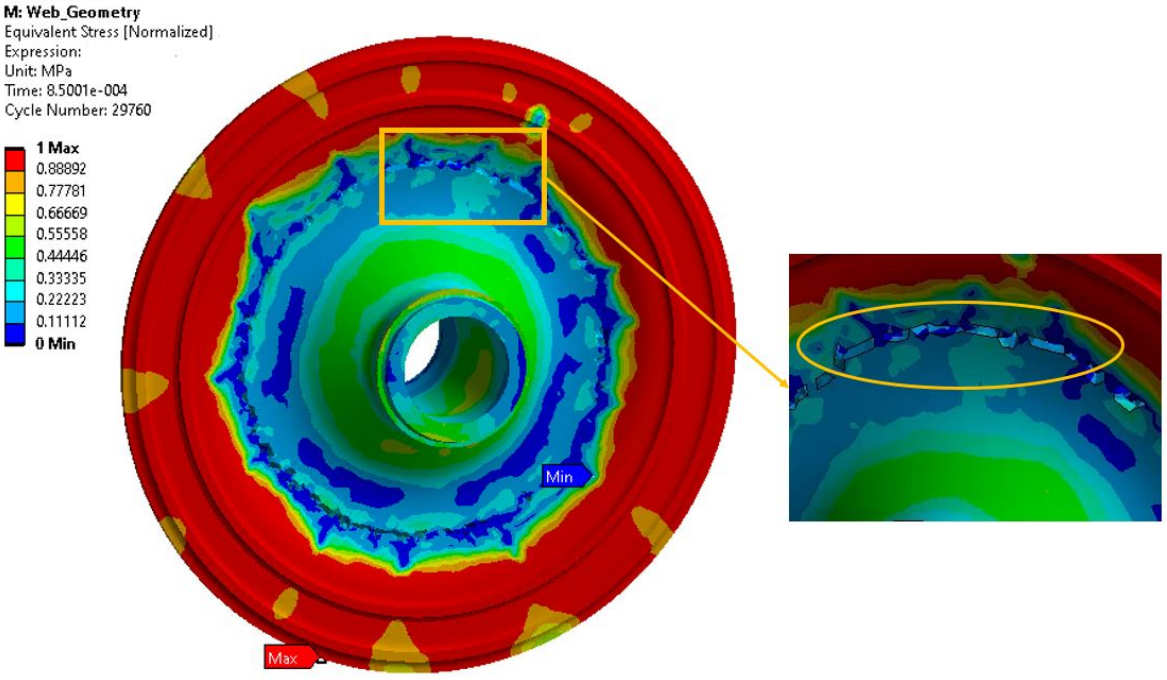

Figure 4.8 Normalized Equivalent Stress (Crack Growth)

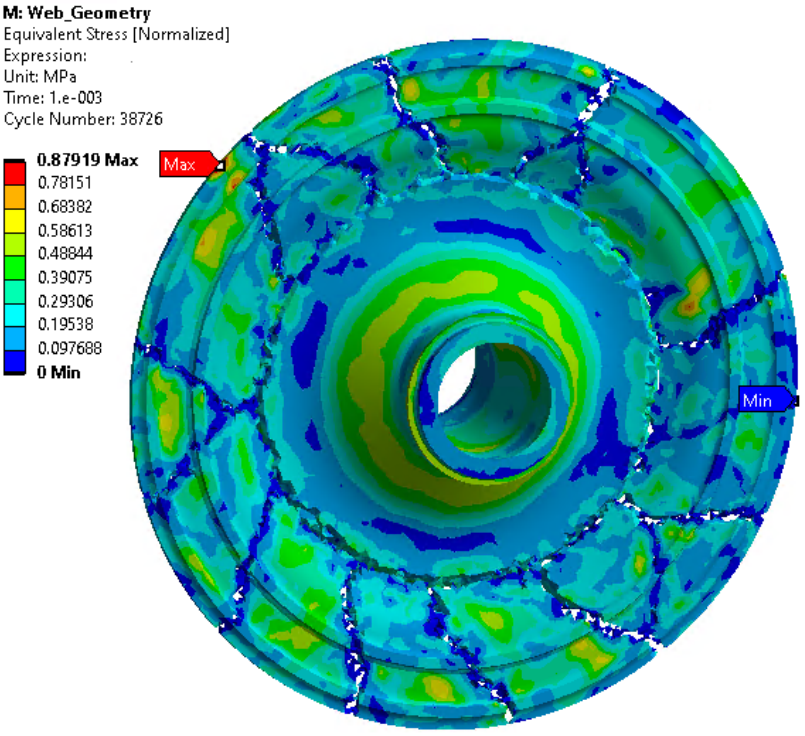

Figure 4.9 Normalized Equivalent Stress (Fracture)

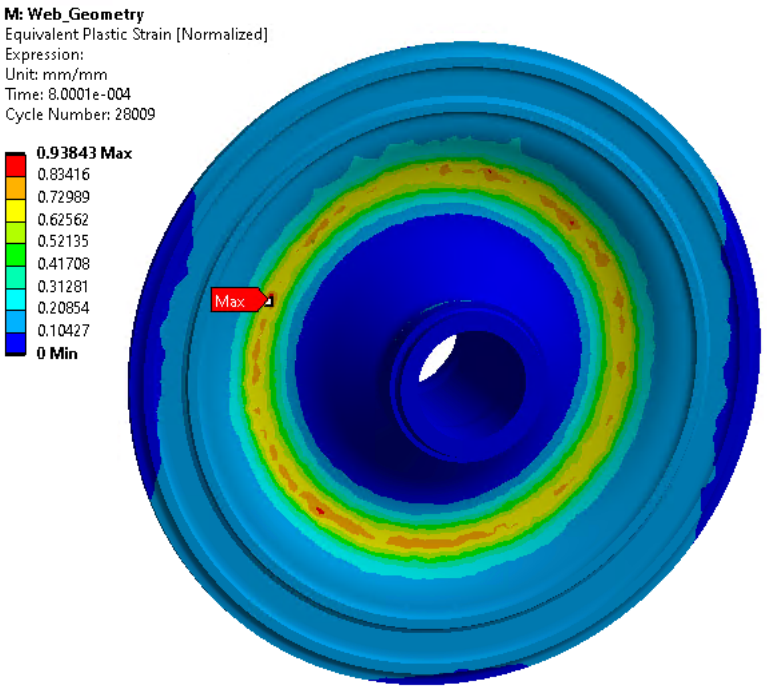

Figure 4.10 Normalized Plastic Strain (Crack Initiation)

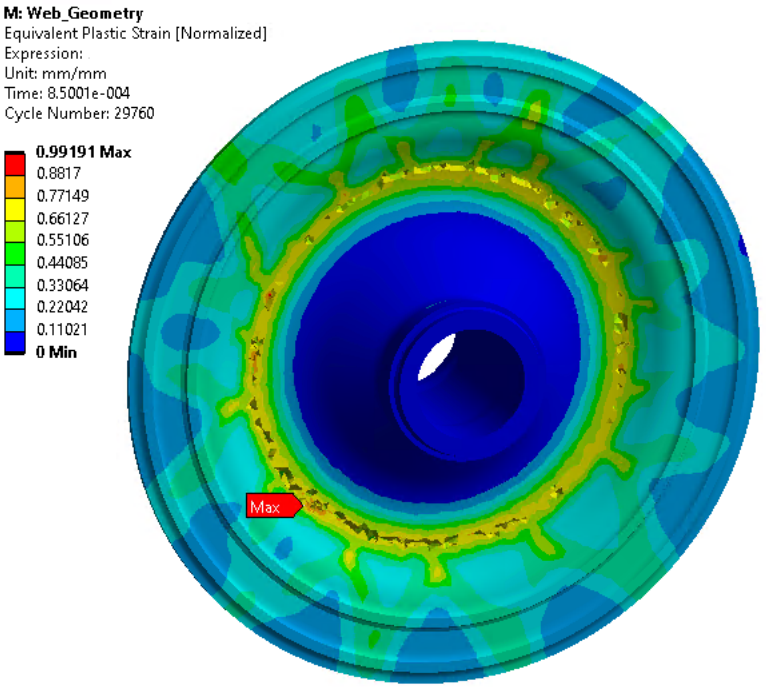

Figure 4.11 Normalized Plastic Strain (Crack Growth)

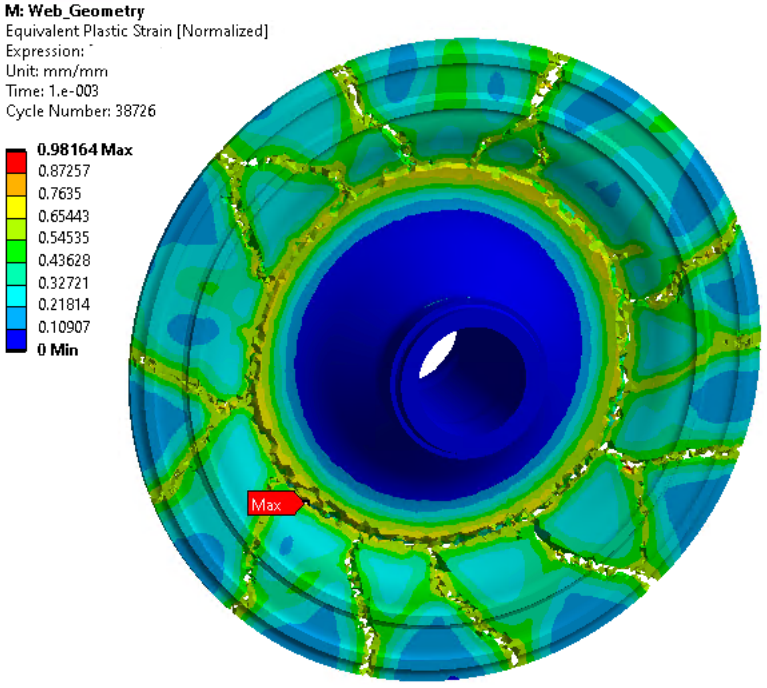

Figure 4.12 Normalized Plastic Strain (Fracture)

4.1.2. Results of Geometry-2

4.1.2.1. Elastic Analysis Results

Normalized stress, strain, and deformation plots are taken from elastic analysis with ω=$\omega_{geo2}^{elastic}$ shared in Figure 4.13-Figure 4.15, respectively. Equivalent stress is the highest stress component, and stress concentration has occurred in the center of the bore region. The radial stress reaches 94.3% of the maximum equivalent stress, which occurred on the web region. Tangential stress is 78.9% of maximum equivalent stress, and the concentration has occurred in the web region.

Maximum total strain arises in the middle of the bore region, and the outer diameter of the part is slightly deformed forward.

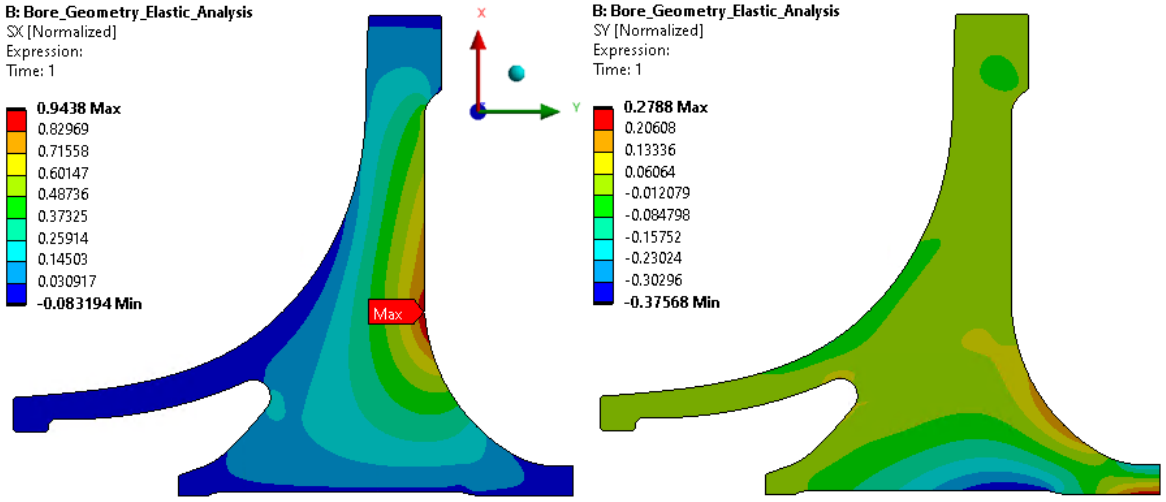

Figure 4.13 Normalized Radial and Axial Stress Plots from Elastic Analysis

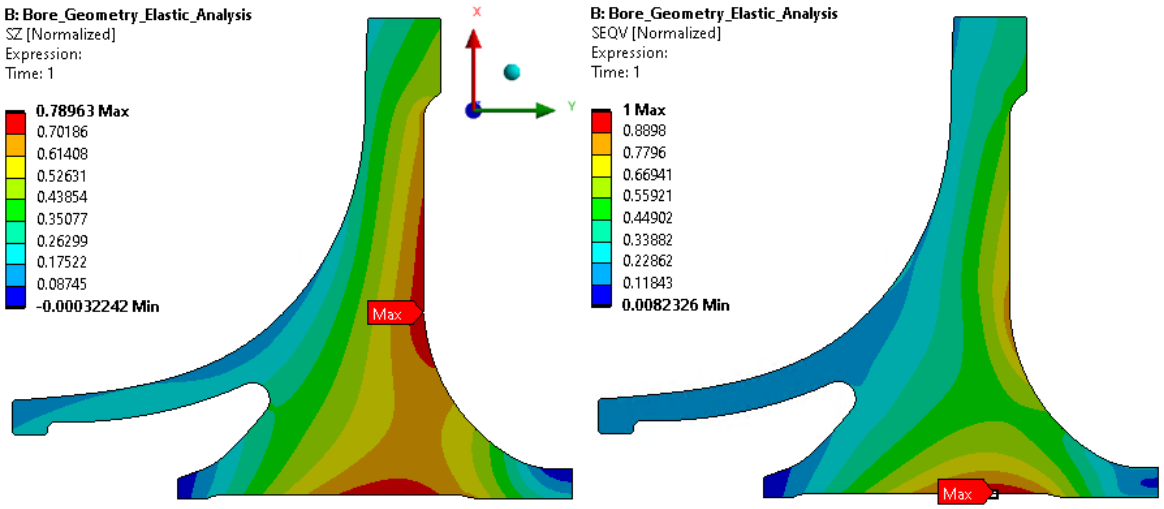

Figure 4.14 Normalized Tangential and Equivalent Stress Plots from Elastic Analysis

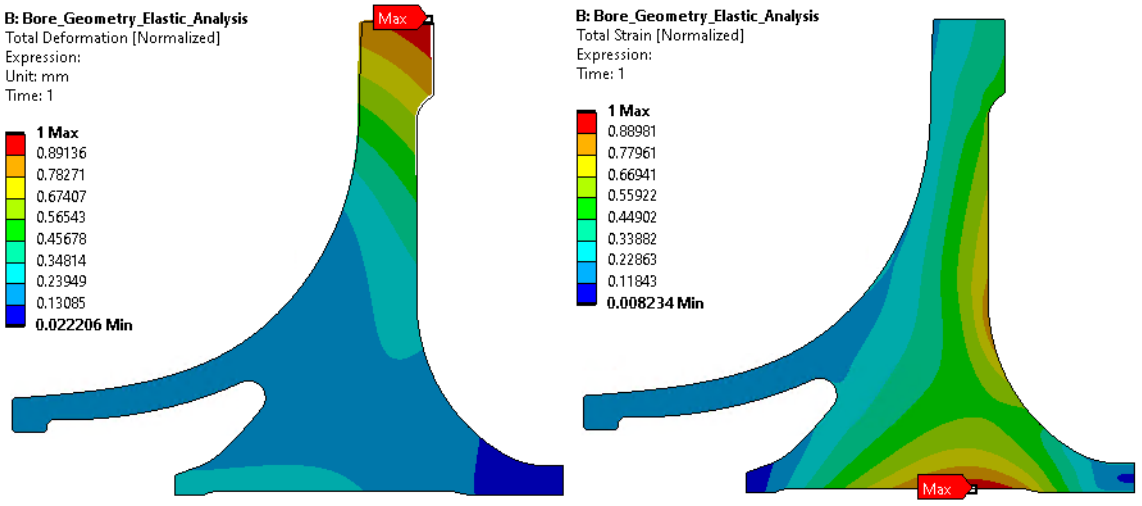

Figure 4.15 Normalized Total Deformation and Total Strain Plots from Elastic Analysis

4.1.2.2. Elastoplastic Analysis Results

Normalized stress, strain, and deformation plots are taken from elastic analysis with ω=$\omega_{geo2}^{plastic}$ shared in Figure 4.4-Figure 4.6. Tangential stress is the highest stress component, and stress concentration occurs in the middle of the part. The equivalent stress reaches 82.5% of the maximum tangential stress and appears in the center of the bore. Radial stress is the lowest stress component and reaches the maximum value on the forward side of the web

region.

The maximum plastic strain arises in the center of the bore region close to the maximum equivalent stress location. The outer diameter of the part is deformed forward, and the bore region is radially elongated.

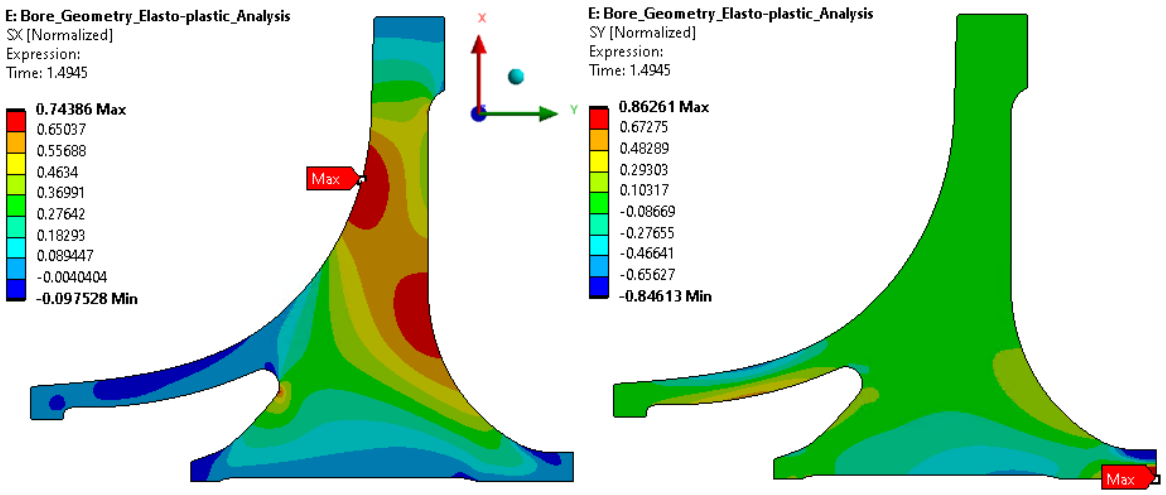

Figure 4.16 Normalized Radial and Axial Stress Plots from Elastoplastic Analysis

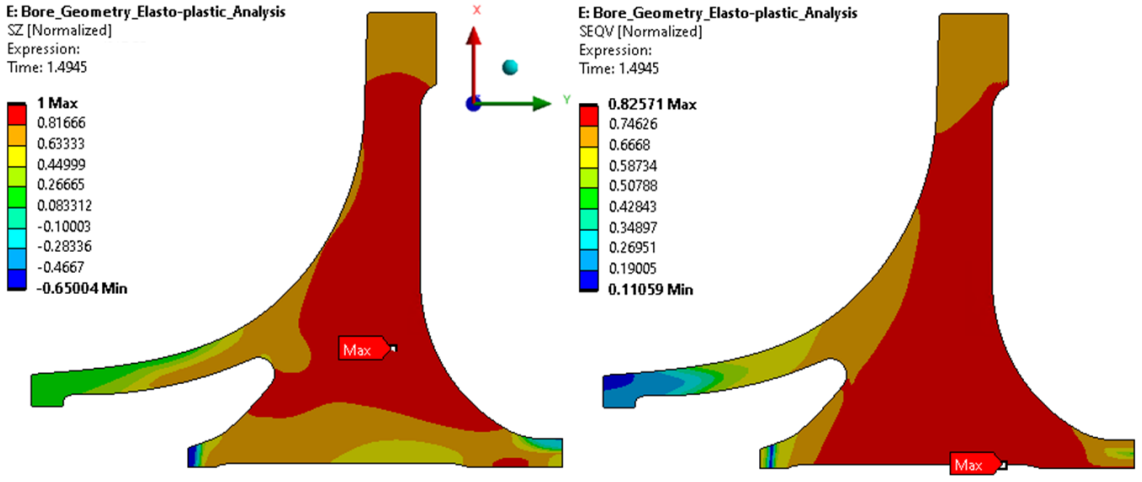

Figure 4.17 Normalized Tangential and Equivalent Stress Plots from Elastoplastic Analysis

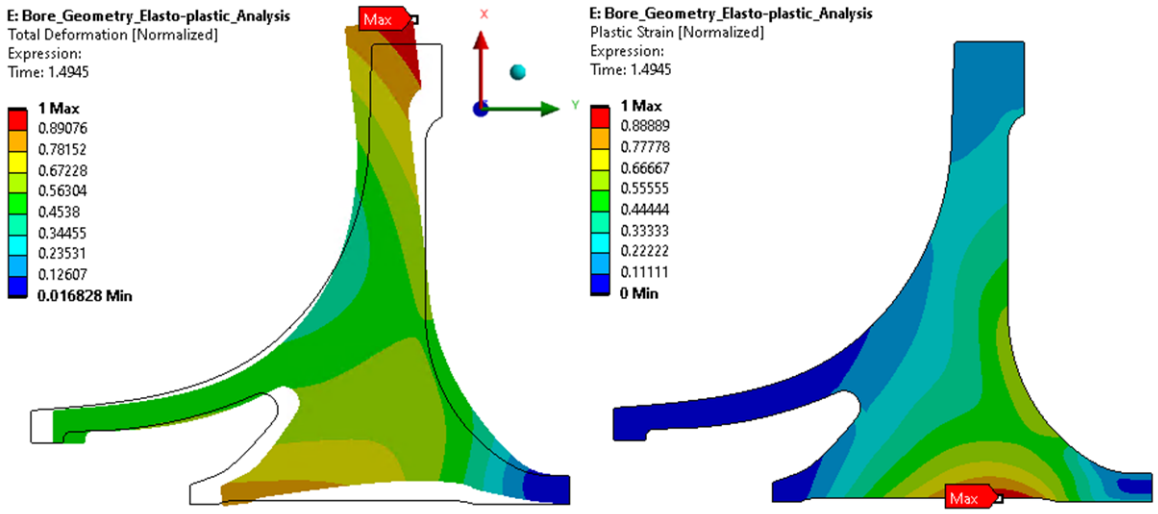

Figure 4.18 Normalized Total Deformation and Total Strain Plots from Elastic Analysis

4.1.2.3. Explicit Dynamic Analysis Results

Normalized equivalent stress and plastic strain plots are taken from explicit dynamic analysis with ω=$\omega_{geo2}^{explicit}$ shared in Figure 56-Figure 61. Crack initiation has occurred in the middle of the bore region and propagated in the radial direction. The equivalent plastic stress reached the maximum value at the fracture.

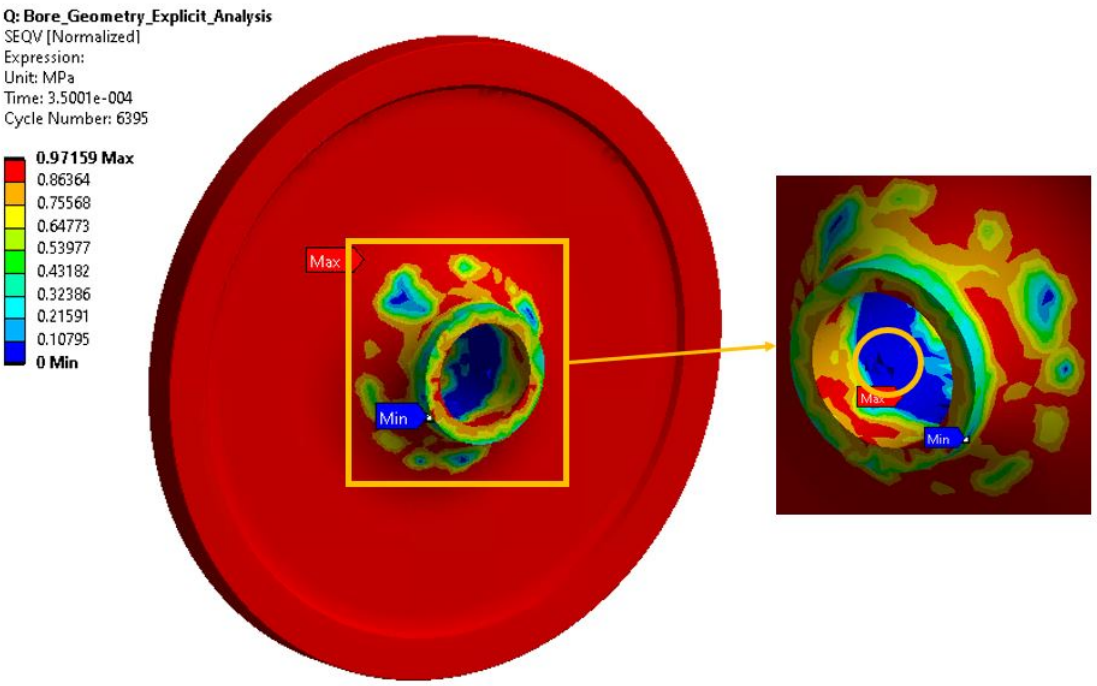

Figure 4.19 Normalized Equivalent Stress (Crack Initiation)

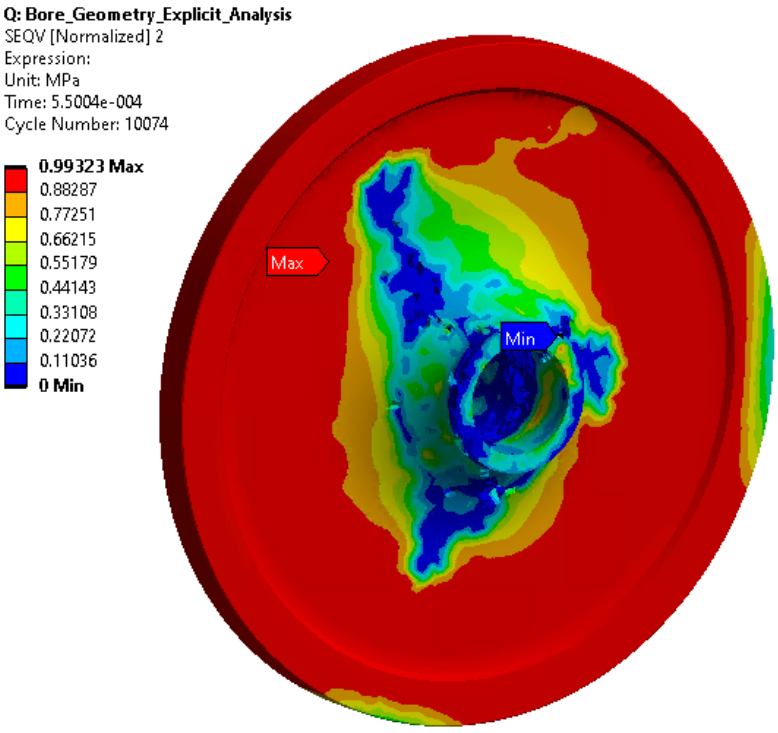

Figure 4.20 Normalized Equivalent Stress (Crack Growth)

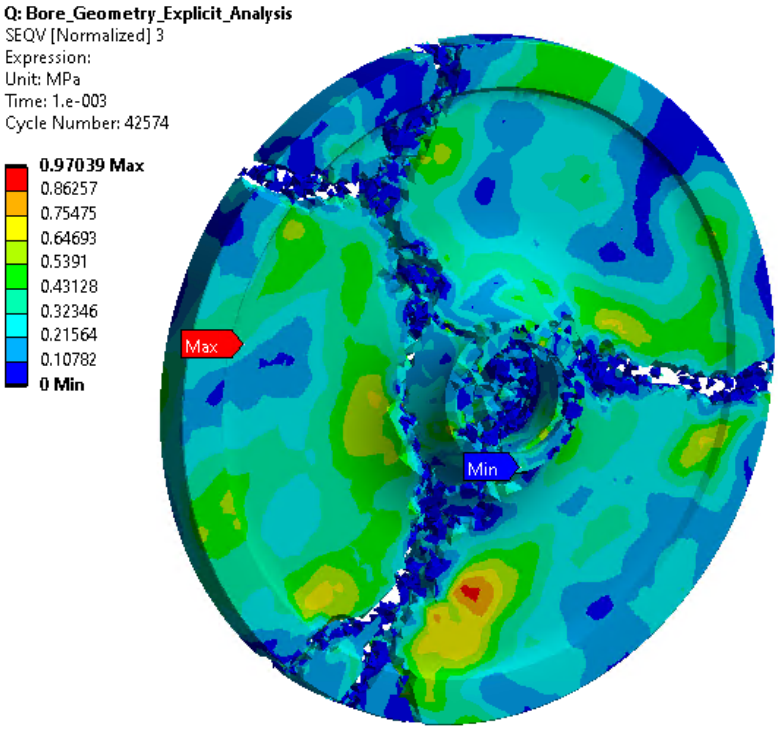

Figure 4.21 Normalized Equivalent Stress (Fracture)

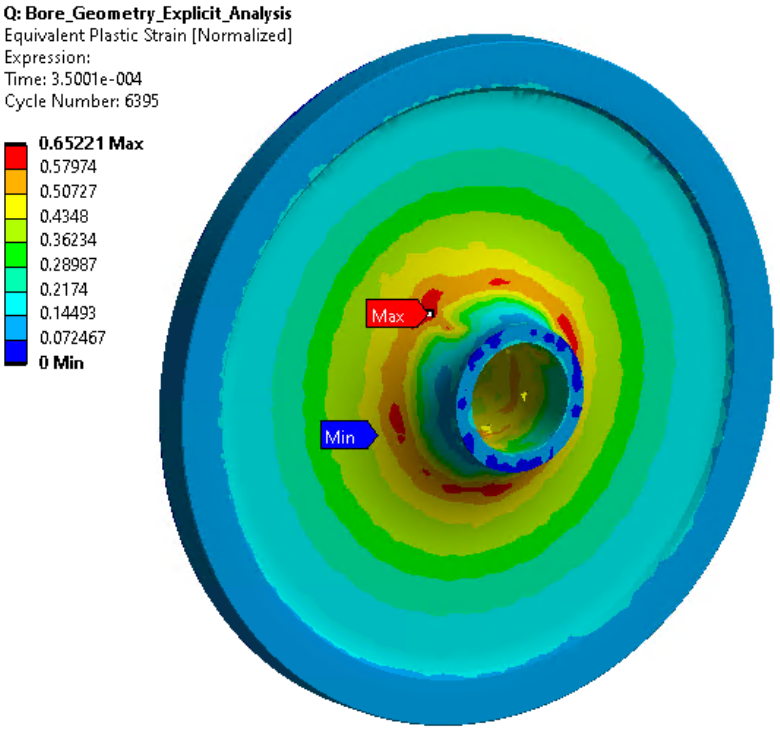

Figure 4.22 Normalized Plastic Strain (Crack Initiation)

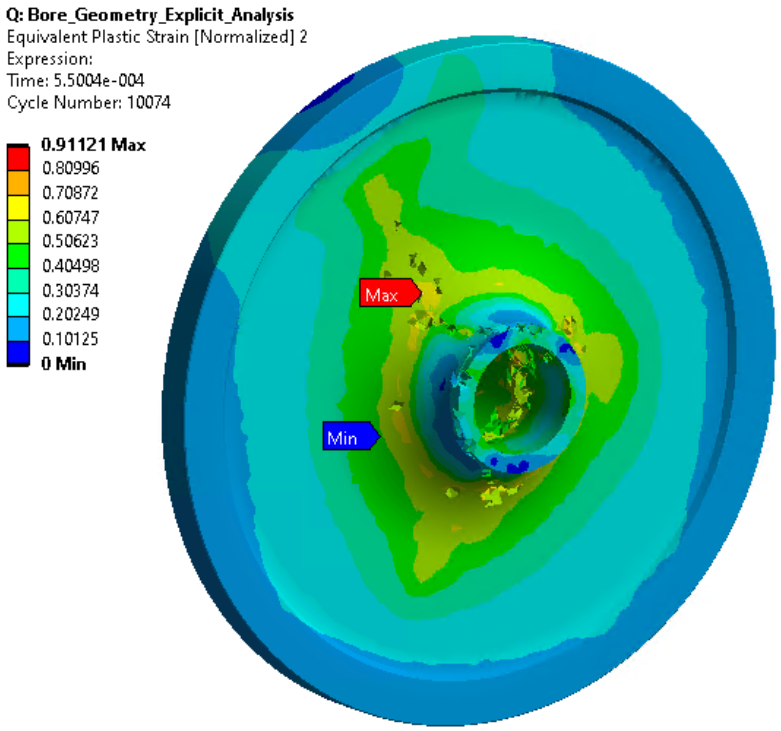

Figure 4.23 Normalized Plastic Strain (Crack Growth)

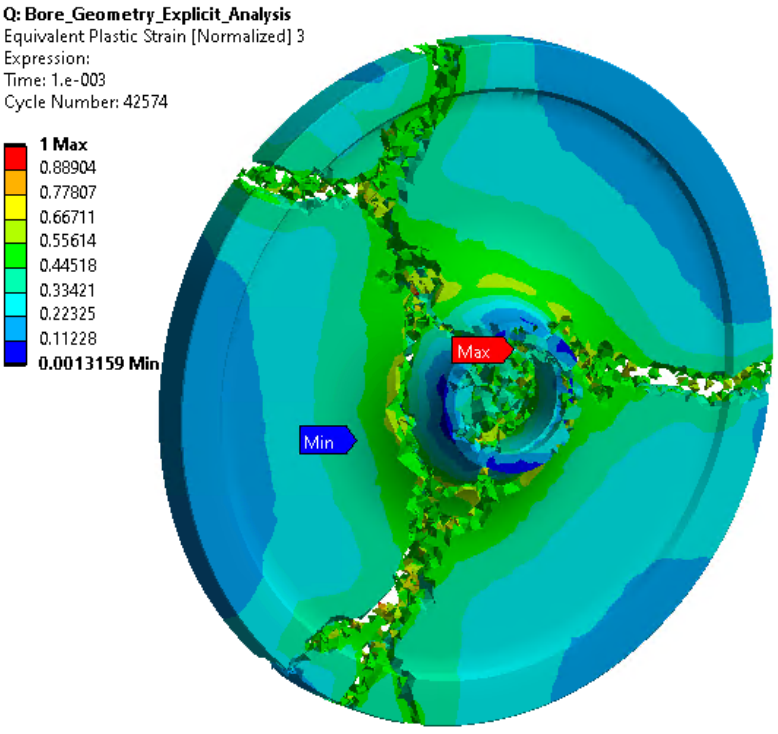

Figure 4.24 Normalized Plastic Strain (Fracture)

4.2. Fracture Criteria Results

Burst speeds are calculated using Robison criteria with Equation 35. The calculated burst speed of Geometry-1 and Geometry-2 are shared below.

$$\omega_{geo1}^{robinson} = 1.768x\omega_{geo1}^{elastic} \tag{37}$$

$$\omega_{geo1}^{robinson} = 1.768x\omega_{geo1}^{elastic} \tag{38}$$

Critical strain distribution on the part is observed in the last three-step before the non-convergence of the elastoplastic analysis. (Figure 4.25 & Figure 4.26) In Geometry-1, the first region that reached critical strain value is the middle of the web region. The strain value increased through the left side of the web region, and the strain value through the cross-section reached a critical value.

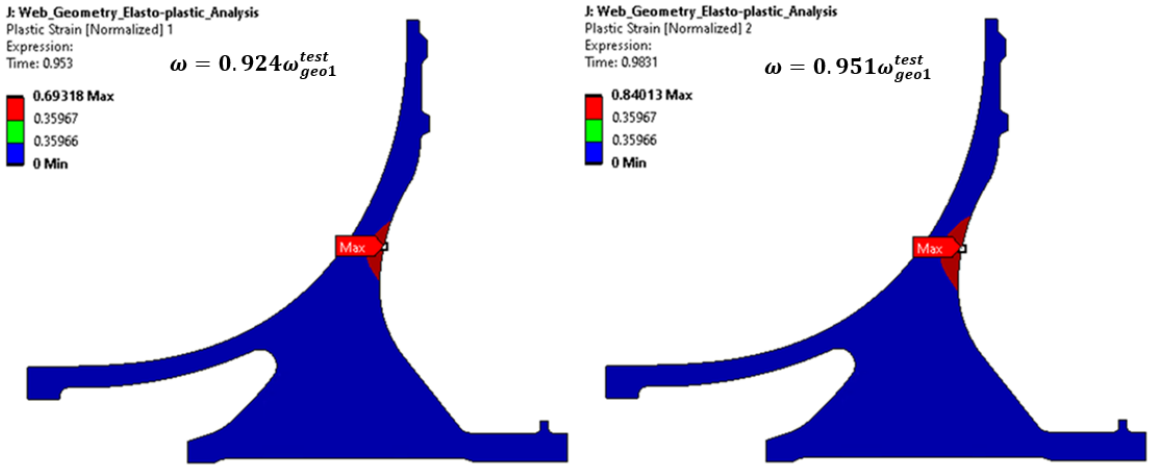

Figure 4.25 Locations Past Critical Strain Value, Geometry-1

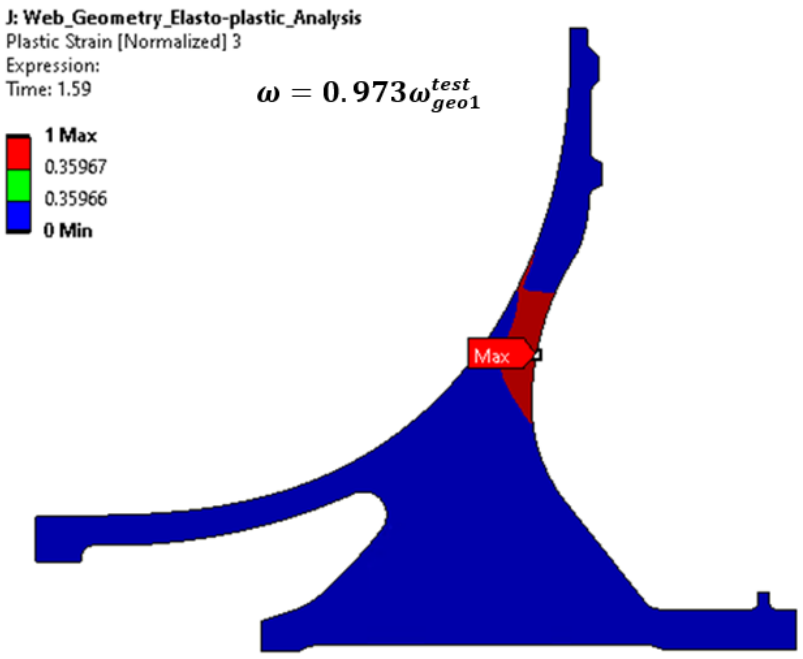

Figure 4.26 Locations Past Critical Strain Value, Geometry-1

The same methodology applied to Geometry-1 is used for Geometry-2. (Figure 4.27 & Figure 4.28) The first region that reached critical strain value is the middle of the bore region. The strain value increased through the backface region, and the strain value through the cross-section reached a critical value.

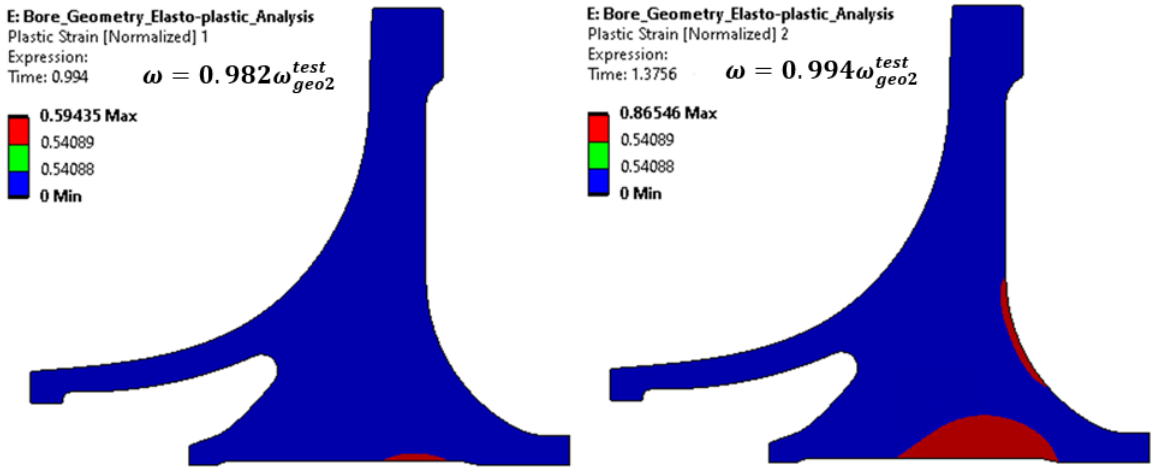

Figure 4.27 Locations Past Critical Strain Value, Geometry-2

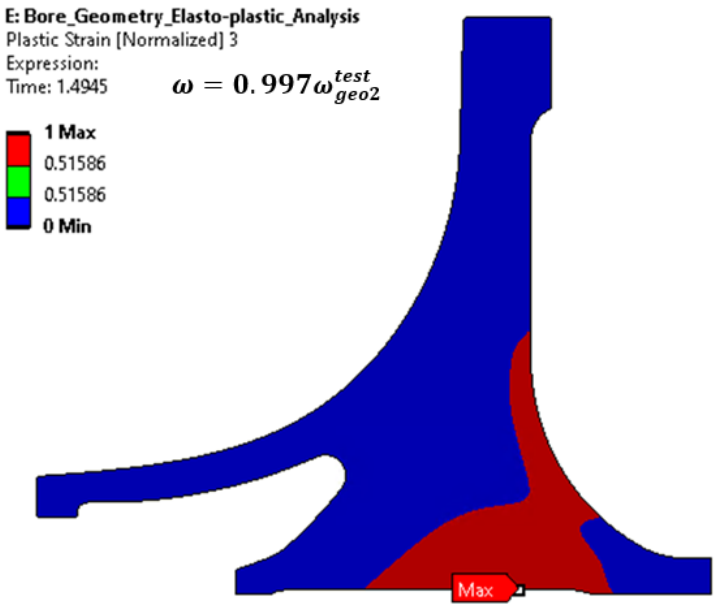

Figure 4.28 Locations Past Critical Strain Value, Geometry-2

The burst speed of Geometry-1 and Geometry-2 are calculated using Robinson, critical strain through cross-section and explicit dynamic analysis criteria and named as $\omega^{robinson}$, $\omega^{plastic}$ and $\omega^{explicit}$. The following sections will share comparisons of numerical results and experimental burst speeds.

4.3. Experimental Results

In this chapter, the experimental results are presented. In addition to the post-burst condition of both geometries, crack initiation, propagation, and fracture moments taken from high-speed camera footage are introduced in Sections 4.3.1. and 4.3.2..

4.3.1. Experimental Results of Geometry-1

Geometry-1 is burst at the web region, and burst speed is denoted as ω_{geo1}^{test}. Photos of burst fragments are shown in Figure 4.29. The high-speed camera footage shows the crack initiation location and crack propagation to the complete burst failure. Crack is initiated on

the web region and propagated in the circumferential direction. Related photos are shared in Figure 4.30 and Figure 4.31. End of the crack propagation, the upper section of the impeller is peeled away from the rest of the part, as in Figure 4.32.

Figure 4.29 Fragments of Geometry-1

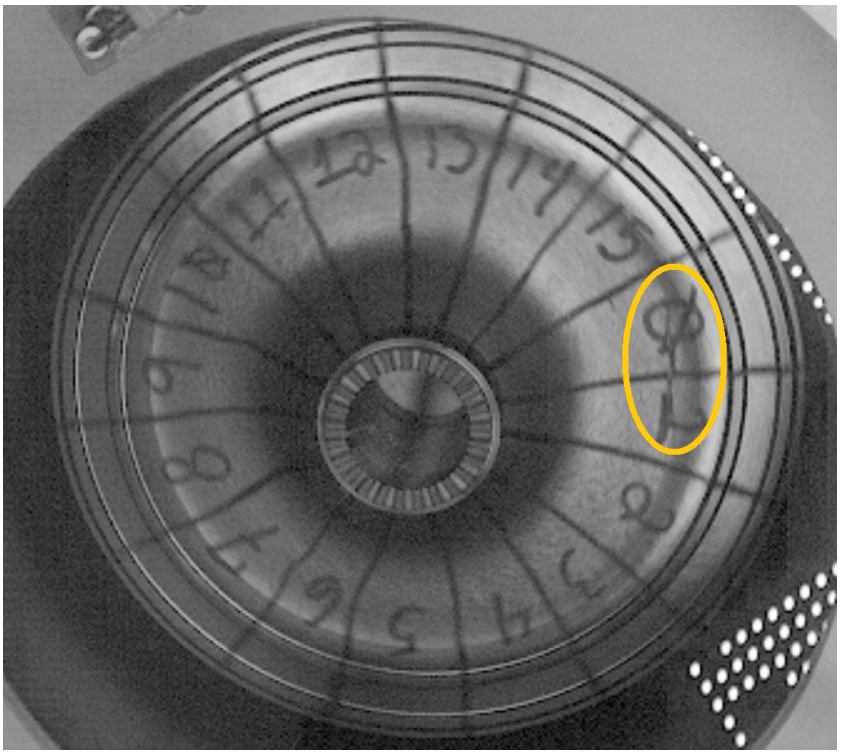

Figure 4.30 Crack Initiation

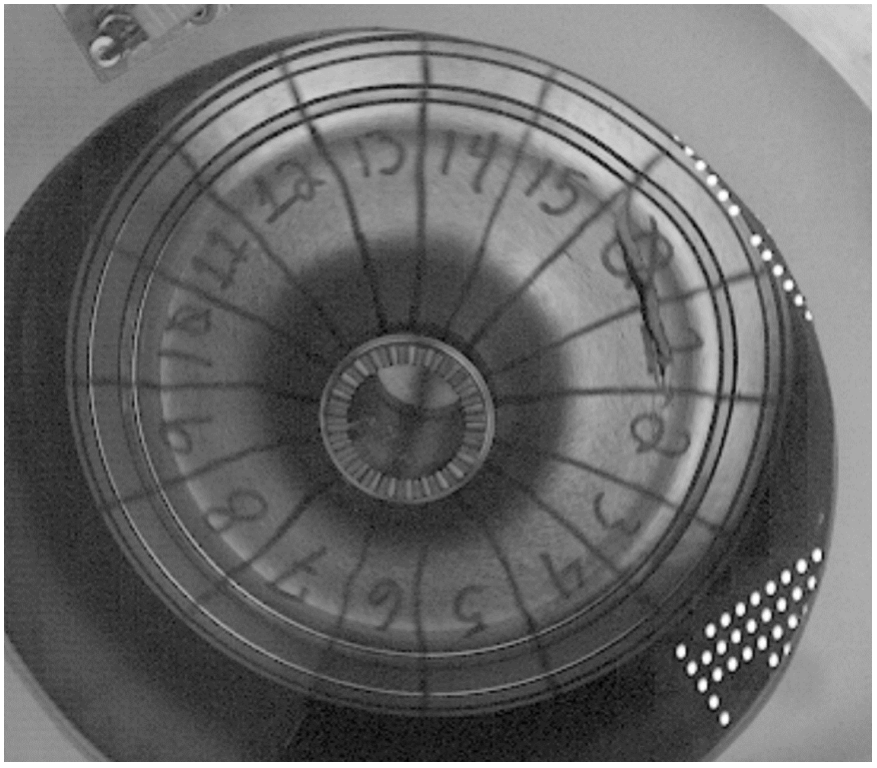

Figure 4.31 Crack Growth

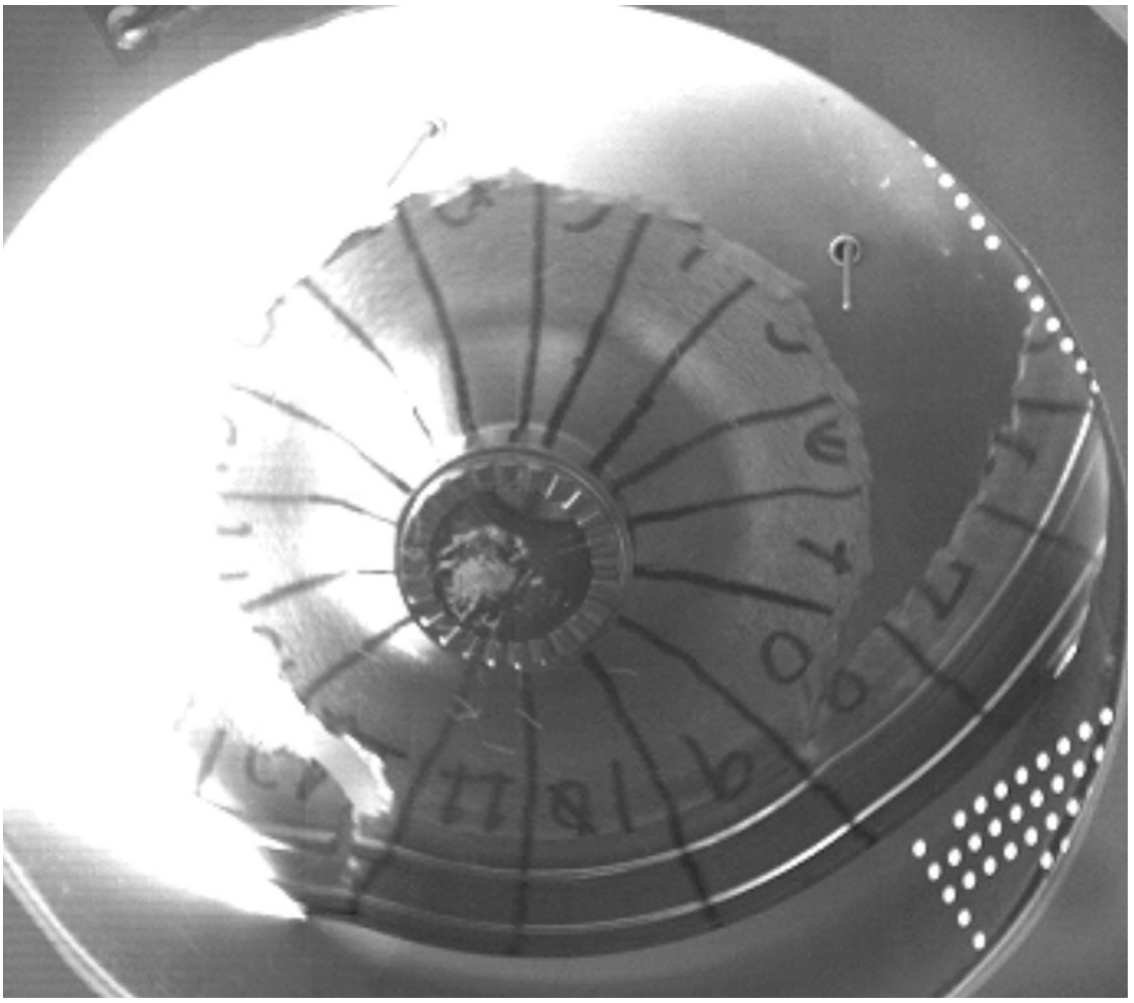

Figure 4.32 Fracture

4.3.2. Experimental Results of Geometry-2

Geometry-2 is burst at the bore region, and the burst speed is denoted as ω_{geo2}^{test}. Photos of burst fragments are shown in Figure 4.33 and Figure 4.34. Crack initiation location and crack propagation to the complete burst failure can be seen in the high-speed camera footage. Crack is initiated on the bore region and propagated in the radial direction. Related photos are shared in Figure 4.35 and Figure 4.36. The end of the crack propagation impeller is divided into two main parts. (Figure 4.37)

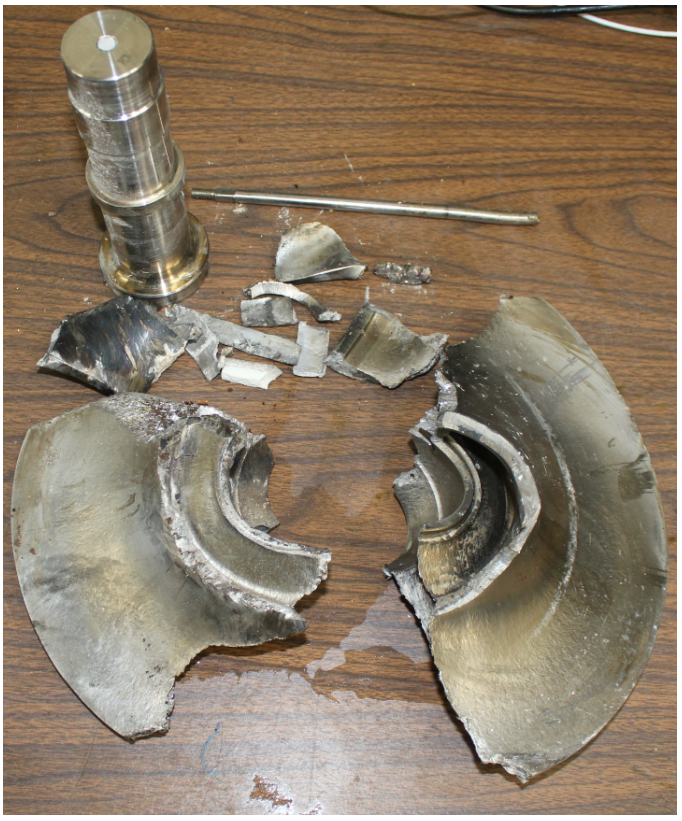

Figure 4.33 Fragments of Geometry-2

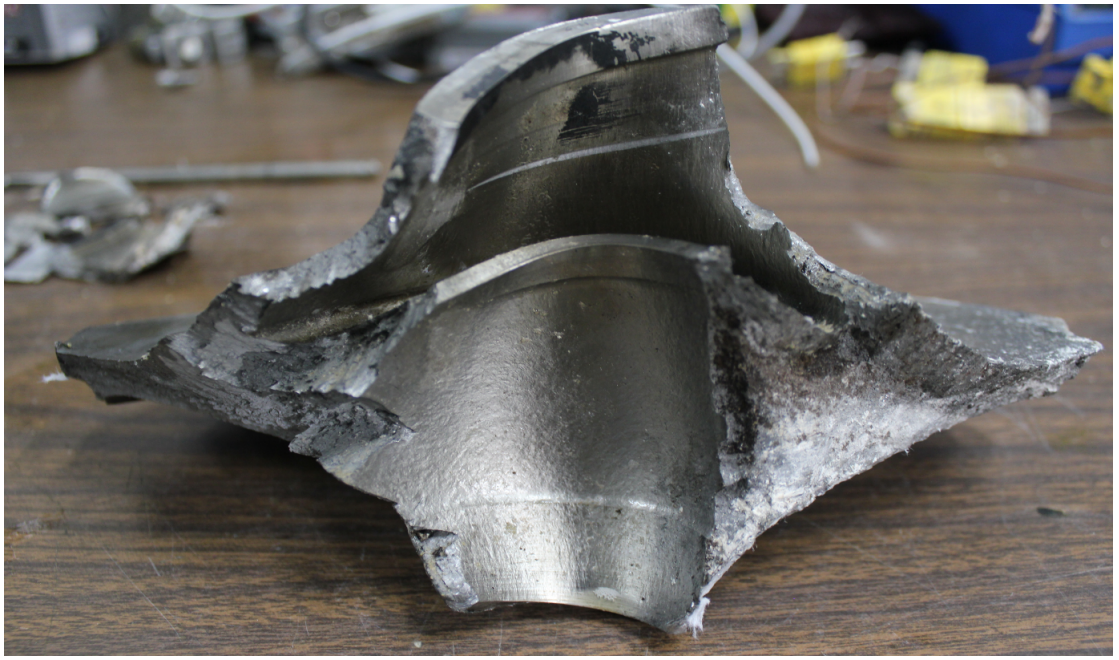

Figure 4.34 Fragments of Geometry-2

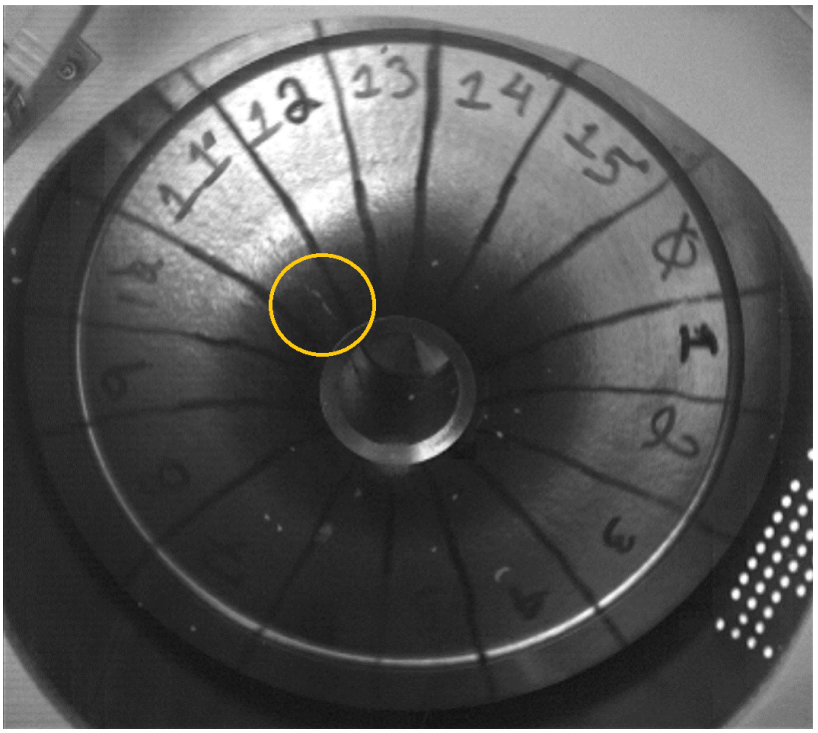

Figure 4.35 First Crack Initiation

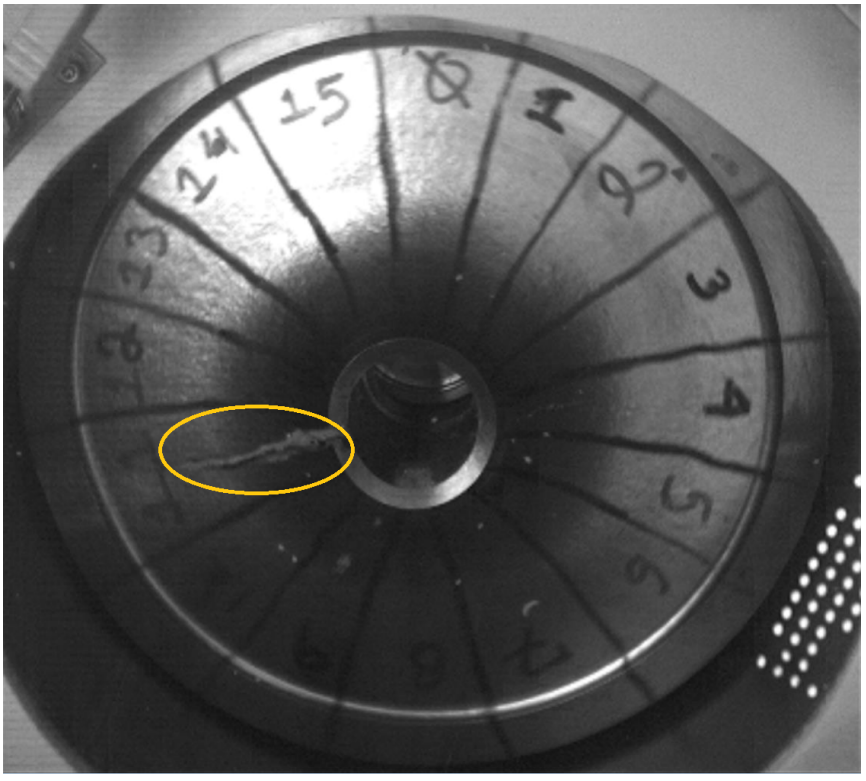

Figure 4.36 Second Crack Initiation

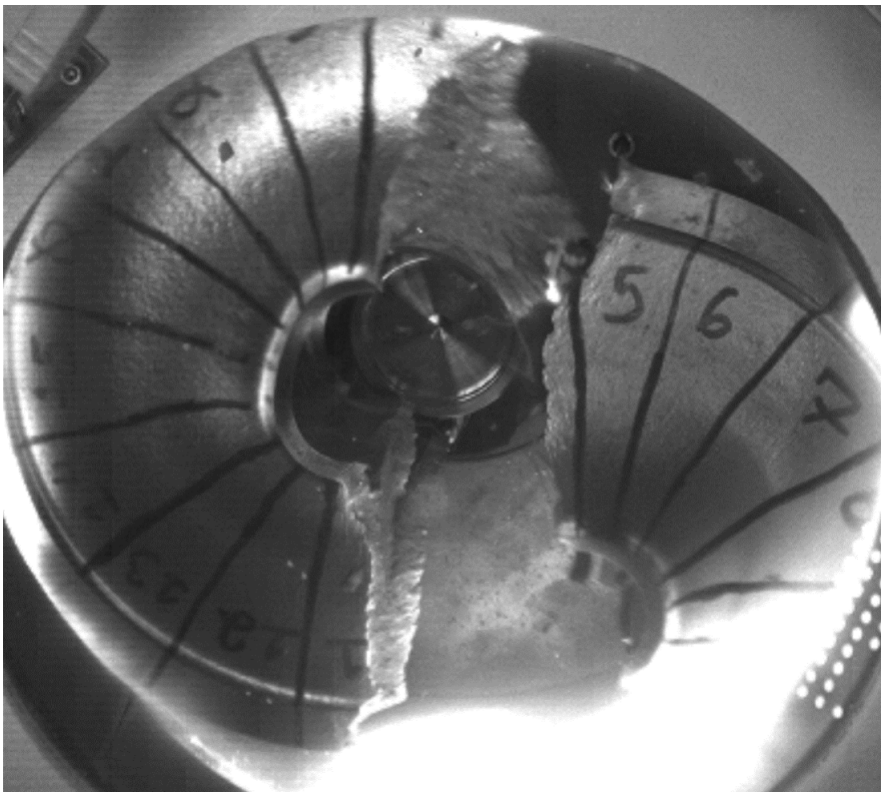

Figure 4.37 Fracture

4.4. Comparison of Numerical and Experimental Results

This chapter shares findings of comparisons of the numerical and experimental results. The comparisons are performed for burst speed and crack initiation, propagation, and fracture characteristics.

4.4.1. Comparison of Results for Geometry-1

All elastic, elastoplastic, and explicit dynamic analyses point to the middle of the web region as burst critical region. In the experimental study, the crack was initiated at a similar location. (Figure 4.38)

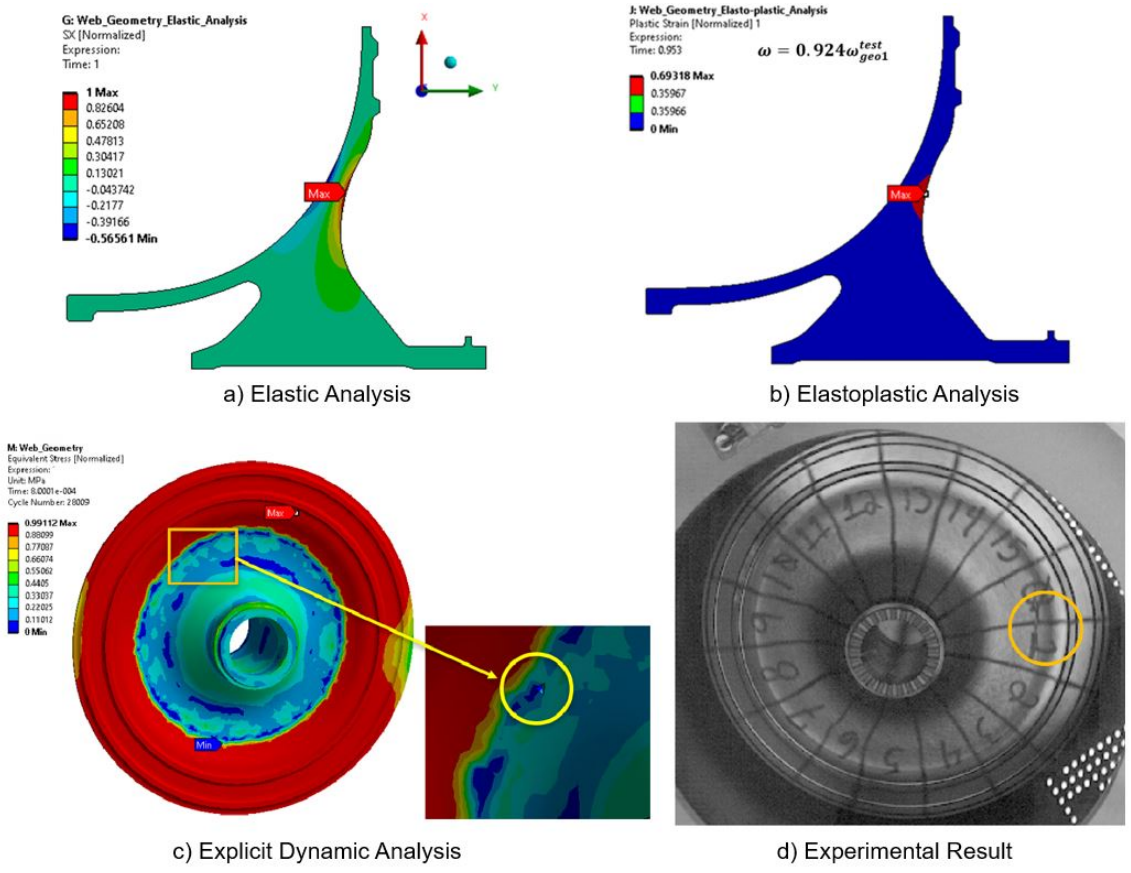

Figure 4.38 Crack Initiation

The elastic analysis does not give additional information about the crack propagation, but when the elastoplastic and explicit dynamic analysis results are examined crack grows through the thickness of the web region. In the high-speed camera footage, it can be observed crack fully develops through the thickness at it first. (Figure 4.39)

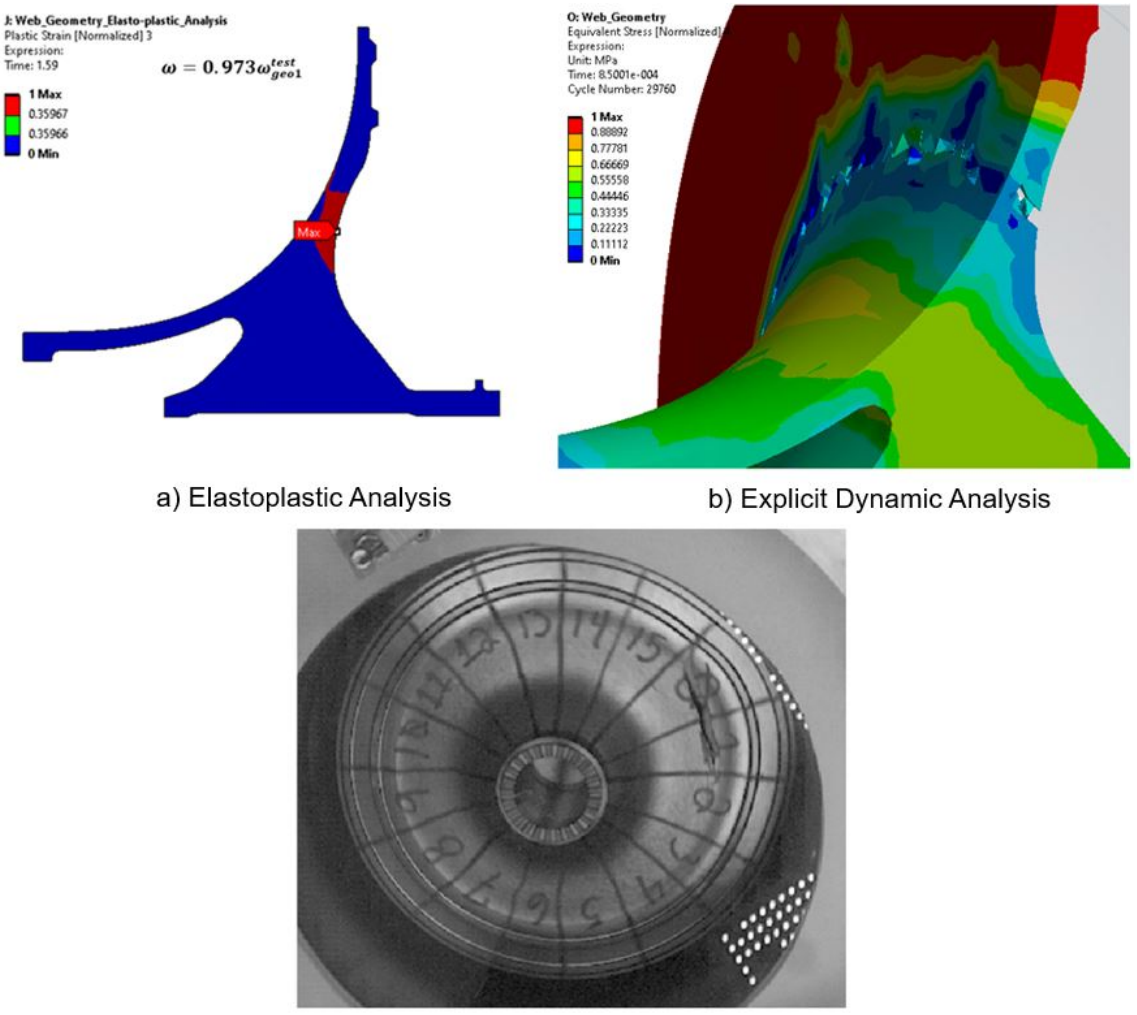

a) Elastoplastic Analysis

b) Explicit Dynamic Analysis

c) Experimental Result

Figure 4.39 Crack Growth

Only explicit dynamic analysis gives information about the burst fracture. The upper section of the disc is peeled away from the rest of the part, and the same behavior is observed in the experimental study. (Figure 4.40)

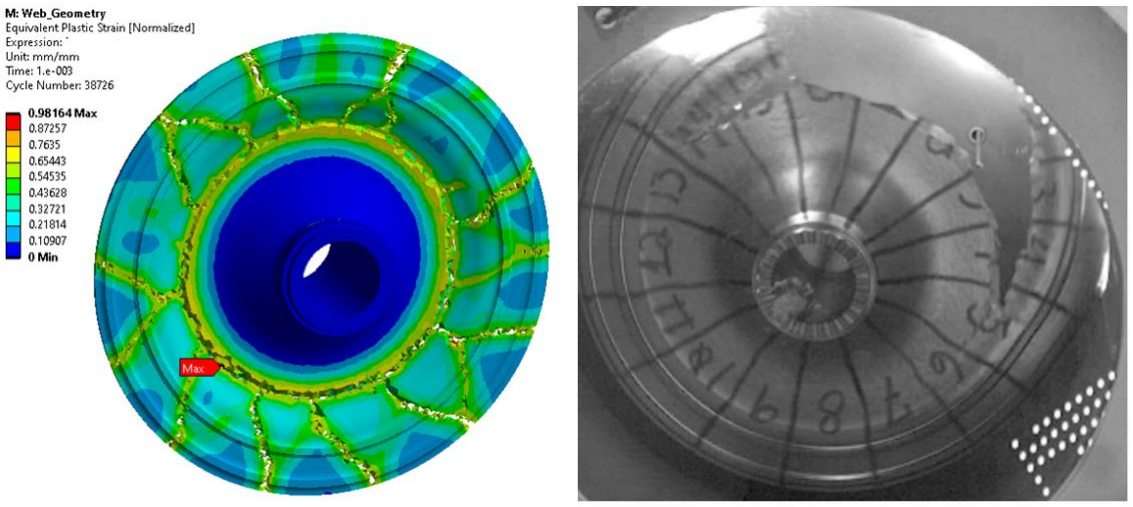

a) Explicit Dynamic Analysis b) Experimental Result

Figure 4.40 Fracture

Lastly, calculated burst speed values of Geometry-1 are divided by experimental burst speed and shared in Table 4.1 The critical strain through cross-section criteria gave the closest value to the experimental burst speed.

Burst Margin Criteria		
Robinson Criteria	$\omega_{geo1}^{robinson}/\omega_{geo1}^{test}$	1.055
Critical Strain Through Cross-section Criteria	$\omega_{geo1}^{plastic}/\omega_{geo1}^{test}$	0.973
Explicit Dynamic Analysis Criteria	$\omega_{geo1}^{explicit}/\omega_{geo1}^{test}$	1.119

Table 4.1 Burst Margin Calculations of Geometry-1

4.4.2. Comparison of Results for Geometry-2

Elastic, elastoplastic, and explicit dynamic analyses showed that the middle of the bore region is the burst critical location. There is a similarity between numerical results, but in the experimental study, the inner region of the bore could not be observed due to the position of the test part. (Figure 4.41)

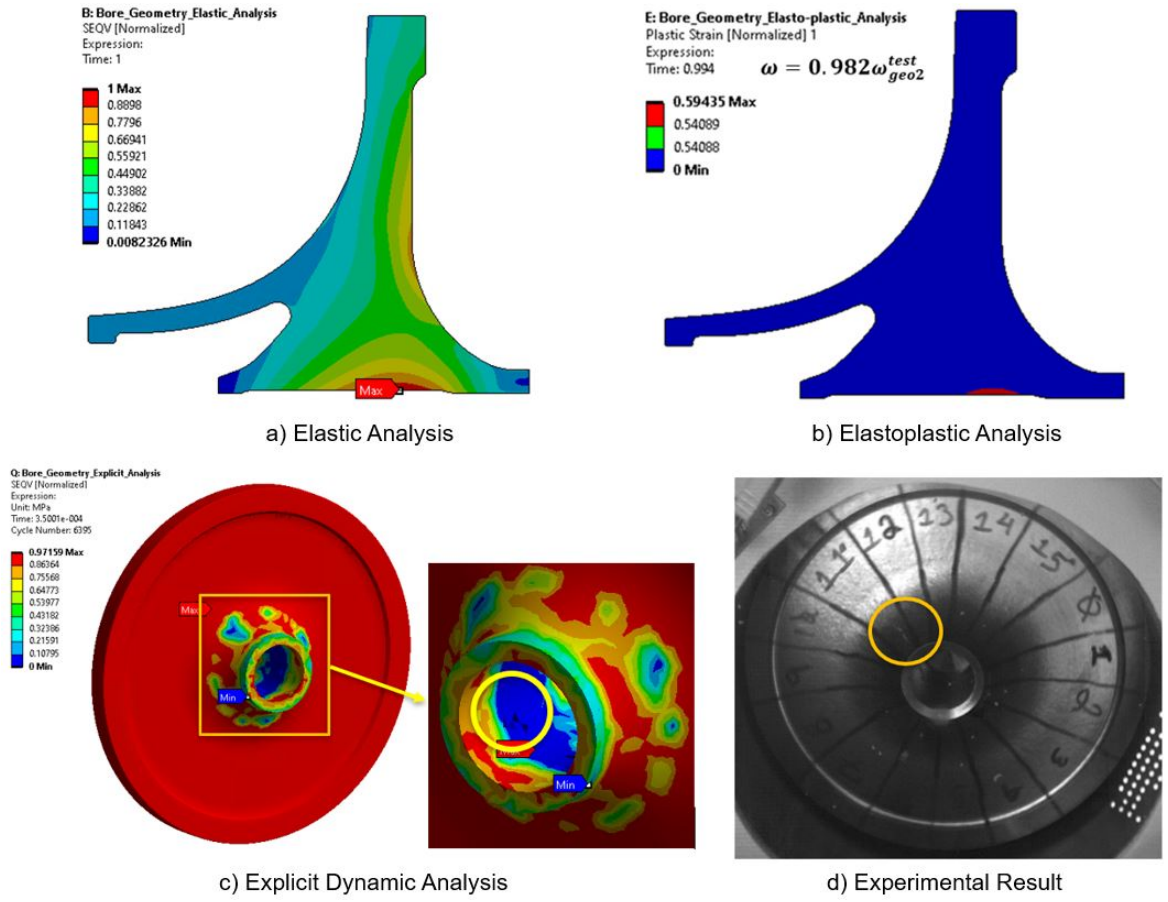

a) Elastic Analysis

b) Elastoplastic Analysis

c) Explicit Dynamic Analysis

d) Experimental Result

Figure 4.41 Crack Initiation

Based on the elastoplastic and explicit dynamic analysis results crack grows through the bore region to the below of the web region. The endpoint of the crack observed in both analyses is similar to that observed in the experimental study. The observed crack in the experimental study can be considered the end point of a crack initiated in the hole region. (Figure 4.42)

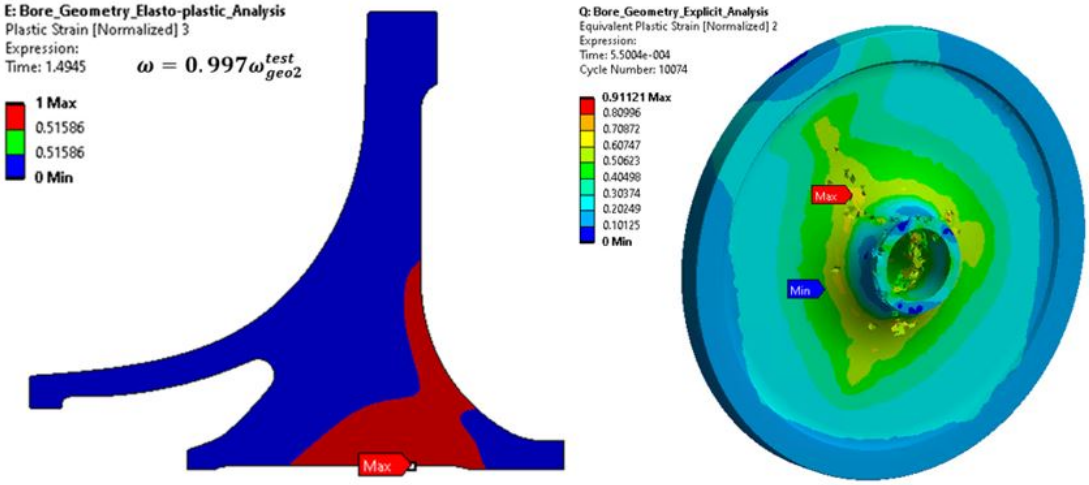

a) Elastoplastic Analysis

b) Explicit Dynamic Analysis

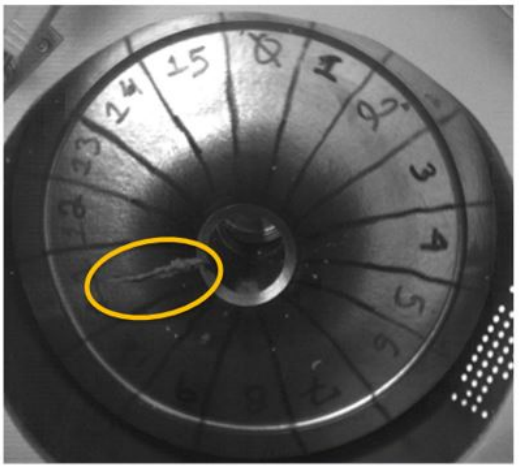

c) Experimental Result

Figure 4.42 Crack Growth

In the explicit dynamic analysis, the crack grew in the radial direction, and the part was divided into three pieces. Similar behavior is observed in the experimental study, except part is divided into two pieces. (Figure 4.43)

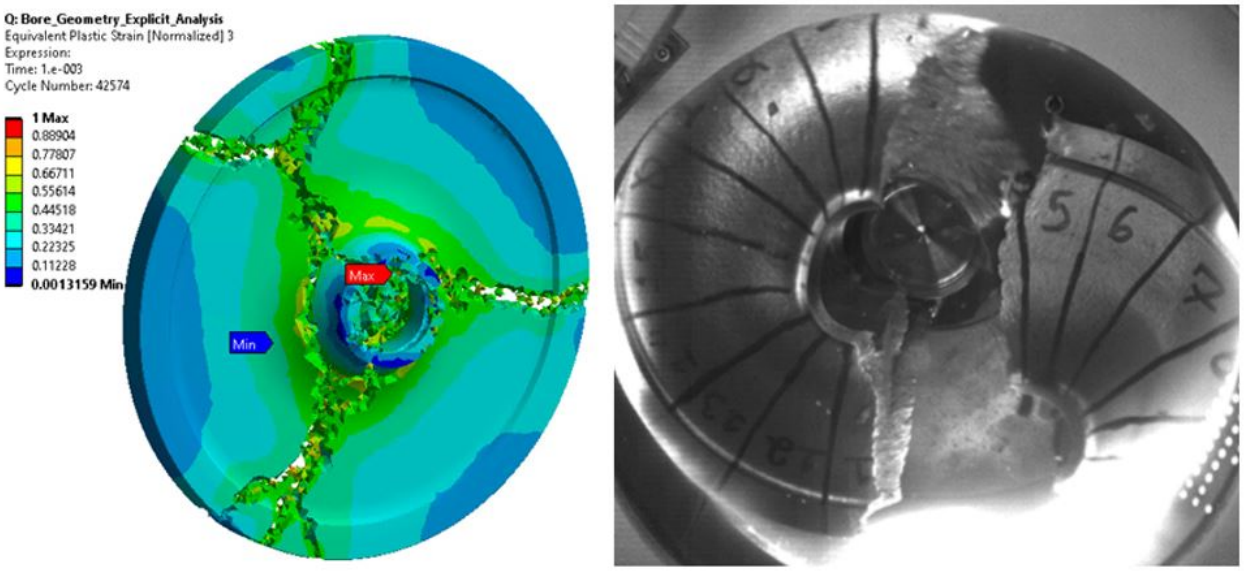

a) Explicit Dynamic Analysis b) Experimental Result

Figure 4.43 Fracture

Finally, calculated burst speed values of Geometry-2 are divided by experimental burst speed and shared in Table 4.2. Again, the critical strain through cross-section criteria gave the closest value to the experimental burst speed.

Burst Margin Criteria		
Robinson Criteria	$\omega_{geo2}^{robinson}/\omega_{geo2}^{test}$	1.030
Critical Strain Through Cross-section Criteria	$\omega_{geo2}^{plastic}/\omega_{geo2}^{test}$	0.997
Explicit Dynamic Analysis Criteria	$\omega_{geo2}^{explicit}/\omega_{geo2}^{test}$	1.269

Table 4.2 Burst Margin Calculations of Geometry-2

5. CONCLUSIONS

In this study, two different impeller geometries are analyzed and tested. Elastic, elastoplastic, and explicit dynamic analyses are performed, and burst speeds are calculated using various fracture criteria based on analysis results. Test geometries are manufactured and tested in a spin test rig. Tests are performed under a uniform 300 °C temperature, and the rotational speed increases until the burst event. Then, the burst event is observed, and the burst speed is recorded. Finally, the findings of the experimental study are compared with the numerical study.

The elastic analyses are performed, and results are used in Robinson's Criteria calculations. Robinson's criteria estimated the burst speed as only +5.5% for Geometry-1 and +3% for Geometry-2. It is provided quick and accurate predictions and can be used in the early design phase.

The elastoplastic analysis is repeated until the non-convergence point, the last point of the analyses used in the study. Critical plastic strain through cross-section criteria is used with the analysis result, and it is observed that this method underestimates burst speed only -2.7% for Geometry-1 and -2.8% for Geometry-2. Critical plastic strain through cross-section criteria is the most accurate method compared with other criteria. The explicit dynamic analyses are repeated with increasing rotational speed until the burst event occurs. This method overestimated the burst speed by +11.9% for Geometry-1 and +26.9% for Geometry-2. This method is less accurate when it is compared with other methods, but it gives additional valuable information about the possible failure location and fracture event.

When the fracture criteria are compared, methods that use elastic analysis results can be used for quick assessment at the beginning of the design phase. Still, if it is desired to obtain more accurate burst speed results, critical strain through cross-section criteria should be chosen. Explicit dynamic analysis criteria overestimated the burst compared to the other two criteria. The elastic analysis gives information about possible crack initiation locations. In addition to the crack initiation, the elastoplastic analysis also shows crack propagation. Finally, the explicit dynamic analysis provides complete information about the crack initiation,

propagation, and burst failure.

REFERENCES

[1] M.P. Boyce. *Gas Turbine Engineering Handbooks*. Gulf Professional Publishing, Oxford, 4 edition, **2012**.

[2] Anonym. Safran arriel 2e. https://www.helis.com/database/engines/Arriel-2E.html, **2022**. Last accessed 02 November 2022.

[3] I. F. Bennett. Khd t117 turbojet engine. http://www.gasturbineworld.co.uk/khdgasturbine.html, **2022**. Last accessed 02 November 2022.

[4] Enes Akca and Ali Gürsel. A review on superalloys and in718 nickel-based inconel superalloy. *Periodicals of Engineering and Natural Sciences (PEN)*, 3, **2015**.

[5] Stefano Chianese. Safety factor against burst speed of turbomachinery rotating disks. **2013**.

[6] Anton N. Servetnik. Energy-based method for gas turbine engine disk burst speed calculation. **2012**.

[7] Anonym. American airlines boeing 767 hpt failure. https://avtales.wordpress.com/2006/06/07/american-airlines-boeing-767-hpt-failure.html, **2006**. Last accessed 02 November 2022.

[8] High bypass ratio turbine engine uncontained rotor events and small fragment threat characterization. Technical report, AIA, **2010**.

[9] Cfr 33.27 - turbine, compressor, fan, and turbosupercharger rotor overspeed. Technical report, Federal Aviation Administration, **2011**.

[10] Cs-e 840 rotor integrity. Technical report, European Union Aviation Safety Agency, **2020**.

[11] Walter Ramberg and William R. Osgood. Description of stress-strain curves by three parameters. **1943**.

[12] Gordon R. Johnson and W. Howard Cook. A constitutive model and data for metals subjected to large strains, high strain rates and high temperatures. **2018**.

[13] Gordon R. Johnson and W. Howard Cook. Fracture characteristics of three metals subjected to various strains, strain rates, temperatures and pressures. *Engineering Fracture Mechanics*, 21:31–48, **1985**.

[14] D.G. Rethwisch and W. D. Callister. *Materials Science and Engineering: An Introduction*, chapter 6. John Wiley and Sons Inc, USA, 10th edition, **2018**.

[15] S.S. Rao. *The Finite Element Method in Engineering*. Elsevier Science and Technology Books, 6th edition, **2018**.

[16] Ansys Inc. Ansys online help. Ansys v16, **2015**.

[17] İ. Güven E. Madenci. *The Finite Element Method and Applications in Engineering Using ANSYS*. Springer International Publishing, 2nd edition, **2015**.

[18] Ansys Inc. Introduction to explicit dynamics. Ansys v19.2, **2018**.

[19] E. Robinson. Bursting tests of steam-turbine disk wheels. In *Trans. ASME 66*, page 373. **1944**.

[20] Y.A. Nozhnitsky and A.N. Servetnik. Prevention of hazardous failure of the turbine rotor due to its overspeed. *IOP Conference Series: Materials Science and Engineering*, 449(1):012025, **2018**.

[21] Standard e-8, standard test methods for tension testing of metallic materials. Technical report, American Society for Testing and Materials, **2022**.

[22] Astm e-21, standard test methods for elevated temperature tension tests of metallic materials. Technical report, American Society for Testing and Materials, **2021**.

[23] Christian Schulze, Markus Dr Weinmann, Christoph Schweigel, Olaf Kessler, and Rainer Bader. Mechanical properties of a newly additive manufactured implant material based on ti-42nb. *Materials*, 11, **2018**.

[24] Hubert W. Meyer and David S. Kleponis. Modeling the high strain rate behavior of titanium undergoing ballistic impact and penetration. *International Journal of Impact Engineering*, 26:509–521, **2001**.

[25] Gregory J. Kay. Failure modeling of titanium-6al-4v and 2024-t3 aluminum with the johnson-cook material model. **2002**.

[26] Ansys Inc. Ansys mechanical apdl element reference. Ansys v14, **2011**.

[27] Albert A. Martino. Designing rotor burst protection. **1971**.